

# Electrical and Optical Characterization of Colloidal Silicon Nanocrystals

A THESIS  
SUBMITTED TO THE FACULTY OF  
UNIVERSITY OF MINNESOTA  
BY

Meng Li

IN PARTIAL FULFILLMENT OF THE REQUIREMENTS  
FOR THE DEGREE OF  
MASTER OF SCIENCE

Russell J. Holmes, Adviser

Dec 2013



## Acknowledgements

My graduate study in University of Minnesota started from fall 2011. At that time, I met with my advisor, Prof. Russell J. Holmes, who granted me the opportunity to do research on hybrid silicon nanocrystal organic light-emitting devices. I was extremely grateful to Prof. Holmes for his mentoring during the recent three years. The discussions with him always inspired me to tackle problems from different angles. With his profound knowledge and dedication in teaching, I not only built a solid background in organic optoelectronics, but also formed a critical way of academic thinking. This thesis would not be possible without Prof. Holmes' kind guidance.

I would also like to express my significant gratitude to the entire Holmes group, including Dr. Kai-Yuan Cheng, Dr. Richa Pandey, Nick Erickson, Matt Menke, Tyler Mullenbach, Yunlong Zou, Nathan Morgan, Dr. Yi Zhang, Tom Fielitz, Ian Curtin and Whitney Kruse for their enormous help and advice both in the laboratory and also in my coursework. The meeting discussions and even everyday talks in the group always broadened my understanding of organic semiconductors and photovoltaics.

I am also grateful to Prof. Uwe Kortshagen, Ting Chen and Jeslin Wu, for their endless support in synthesizing the silicon nanocrystal materials used in this work, and for insightful discussions regarding my research. This collaboration was beneficial for me to develop communication skills and technical knowledge that extends beyond silicon nanocrystals. I would also like to acknowledge Prof. C. Daniel Frisbie and his research group. In particular, I would like to thank Dr. Wei Xie, Yanfei Wu and Dr. Zuoti Xie for training and helping me utilize tools in the Frisbie laboratory for the completion of my

research. I would also thank Prof. Aaron Massari for his generosity in permitting me to utilize his liquid nitrogen optical cryostat.

In addition, I would like to thank all of my friends who supported me during my graduate study in the University of Minnesota. Their names are (please forgive me if I forgot to mention your name): Yunlong Zou, Tuoqi Li, Yutao Tao, Peng (Andrew) Xu, Han Zhang, Dandan Xu, Weihua Li, Jincheng Zhou, Liangliang Gu, Boxin Tang, Lian Bai, Dr. Sipei Zhang, Jing Han, Jie Lu, Peng Bai and all the others in the US and in China. Without their kind help in everyday life, my living in the US would not have been as easy and happy.

Finally, I would like to thank my entire family. My parents, Muqin Li and Yaorong Li, both supported my trip to the US and kept in contact with me. Even if I met some downfalls in my life, I could always feel that my parents stand on my side. My grandparent, Xiuying Wang, and other relatives also provided a warmly welcome to me during my vacation back to China. Their efforts saved me from getting homesick and made me more confident during my graduate study.

## **Dedication**

*This thesis is dedicated to my parents, Muqin Li and Yaorong Li, for their endless love of supporting me, believing in me, and teaching me the spirit of diligence and perseverance during my life.*

## **Abstract**

Colloidal silicon nanocrystals (SiNCs), due to their high photoluminescence efficiency and tunable bandgap, can be used to fabricate highly efficient hybrid nanocrystal-organic light-emitting-devices (NC-OLEDs) that emit in red or near infrared spectrum. Despite reports of outstanding device performance, the underlying mechanism of this high efficiency remains unknown. Consequently, this thesis focuses on studying the electrical and optical properties of SiNCs. The electrical conductivity and mobility of electrons and holes are successfully extracted in order to explain the observed dependence of device efficiency on SiNC surface ligand coverage. Steady-state and transient photoluminescence is also examined to better understand the connection between surface ligand coverage and molecular photophysics. In addition, these measurements are used to better understand the mechanisms for non-radiative exciton decay in SiNCs. This work elucidates the relationship between SiNC properties and device performance, potentially guiding the design of future NC materials for high performance.

## Table of Contents

<b><u>Acknowledgements</u></b> .....	i
<b><u>Dedication</u></b> .....	iii
<b><u>Abstract</u></b> .....	iv
<b><u>Table of Contents</u></b> .....	iv
<b><u>List of Tables</u></b> .....	vii
<b><u>List of Figures</u></b> .....	viii
<b><u>Chapter 1 Introduction to Semiconductor Nanocrystals</u></b> .....	1
1.1 Introduction .....	1
1.2 Scope of This Thesis .....	2
1.3 Introduction to Silicon Nanocrystals .....	2
1.4 Quantum Confinement in Nanocrystals .....	4
1.4.1 Introduction to Quantum Confinement Effect .....	4
1.4.2 Quantum Mechanical Model of Confinement .....	6
1.5 Charge Carrier Transport in Nanocrystals .....	8
1.6 Exciton Generation and Recombination in Nanocrystals .....	11
<b><u>Chapter 2 Introduction to Hybrid Nanocrystal-Organic Light-Emitting Devices</u></b> .....	16
2.1 Introduction .....	16
2.2 Operating Mechanism of Hybrid SiNC-OLEDs .....	19
2.3 External Quantum Efficiency of Hybrid SiNC-OLEDs .....	20
2.4 Motivation of This Thesis .....	22
<b><u>Chapter 3 Experiment Procedures</u></b> .....	24
3.1 Synthesis and Functionalization of Silicon Nanocrystals .....	24
3.1.1 Non-thermal Plasma Synthesis of Silicon Nanocrystals .....	24
3.1.2 Functionalization of Silicon Nanocrystals .....	25
3.2 Electrical Characterization .....	26
3.2.1 Current-Voltage Measurements .....	26
3.2.2 Time-of-Fight Mobility Measurements .....	28
3.3 Optical Characterization .....	29
3.3.1 Room Temperature Steady-state Photoluminescence .....	29
3.3.2 Room Temperature Transient Photoluminescence .....	30
3.3.3 Temperature Dependent Steady-state and Transient Photoluminescence .....	30
<b><u>Chapter 4 Charge Transport in Silicon Nanocrystals</u></b> .....	32
4.1 Foreword .....	32
4.2 Electrical Conductivity in Silicon Nanocrystals .....	32
4.3 Carrier Mobility in Silicon Nanocrystals .....	35
4.4 Summary .....	40
<b><u>Chapter 5 Silicon Nanocrystal Photoluminescence</u></b> .....	41
5.1 Foreword .....	41
5.2 Room Temperature Photoluminescence .....	42
5.3 Temperature Dependent Photoluminescence .....	45
5.3.1 Steady-state Photoluminescence .....	45

5.3.2 Transient Photoluminescence .....	49
5.4 Summary .....	51
<b><i><u>Chapter 6 Conclusion and Future Research Proposal</u></i></b> .....	53
6.1 Conclusion .....	53
6.2 Charge Mobility using Lateral Patterned Devices .....	54
6.3 Spin Fraction in Hybrid SiNC-OLEDs .....	56
6.3.1 Exciton Spin Fraction Measurement .....	56
6.3.2 Possible Mechanisms For High Spin Fraction .....	60
6.4 Exciton Transfer in Silicon Nanocrystals .....	64
6.5 Afterword .....	68
<b><i><u>References</u></i></b> .....	69
<b><i><u>Appendix</u></i></b> .....	83
A.1 Structures of Chemicals Mentioned in This Thesis .....	83

## List of Tables

<b>Table 2.1</b> Summary of the progress of NC-OLEDs in the visible emission range .....	17
<b>Table 2.2</b> Summary of reported near-infrared-nanocrystal electroluminescence .....	18
<b>Table 3.1</b> Calculation of surface SiNC atom capping ratio.....	26
<b>Table 4.1</b> Electron conductivity and Poole-Frenkel coefficient for 1:5 SiNCs .....	34
<b>Table 4.2</b> Summary of 1:5, 1:1000 and 1:2000 SiNC electron and hole mobilities .....	38
<b>Table 5.1</b> Summary of steady-state and transient PL at room temperature .....	43
<b>Table 5.2</b> Energy bandgap and average phonon energy of 3 nm and 5 nm SiNCs.....	47
<b>Table 5.3</b> Decay rates and activation energy of 3 nm and 5 nm SiNCs .....	51

## List of Figures

<b>Figure 1.1</b> Photographs of visible light emission from SiNCs.....	3
<b>Figure 1.2</b> Size dependent absorption and photoluminescence spectra of CdSe NCs.....	5
<b>Figure 1.3</b> Density of states of a semiconductor as a function of dimensionality .....	5
<b>Figure 1.4</b> Schematic plot of a spherical nanoparticle embedded in a dielectric medium.	7
<b>Figure 1.5</b> Comparison of theoretical and experimental energy bandgap in CdSe NCs ..	8
<b>Figure 1.6</b> Energy band diagram for electron- and hole-only devices.....	8
<b>Figure 1.7</b> Current-voltage characteristics for CdSe NC devices.....	11
<b>Figure 1.8</b> Generation and recombination mechanisms in bulk semiconductors .....	12
<b>Figure 1.9</b> Room temperature energy band diagram for bulk Si .....	13
<b>Figure 2.1</b> Tunable energy bandgap of nanocrystals .....	18
<b>Figure 2.2</b> Structure of a hybrid SiNC-OLED.....	19
<b>Figure 2.3</b> Energy band diagram of a SiNC-OLED.....	20
<b>Figure 2.4</b> Light out-coupling losses in OLEDs .....	20
<b>Figure 2.5</b> Illustration of four possible exciton spin combinations.....	22
<b>Figure 2.6</b> External quantum efficiencies of SiNC-OLEDs .....	23
<b>Figure 3.1</b> Non-thermal plasma synthesis and functionalization of SiNCs .....	24
<b>Figure 3.2</b> Transmission electron micrograph of SiNCs.....	25
<b>Figure 3.3</b> Functionalization mechanism in SiNCs .....	25
<b>Figure 3.4</b> Scanning probe microscopy thickness scan in a SiNC device .....	27
<b>Figure 3.5</b> Experimental setup for time-of-flight mobility measurements of SiNCs.....	28
<b>Figure 3.6</b> PL efficiency measurement and spectra of SiNC thin films .....	29
<b>Figure 3.7</b> Room temperature transient photoluminescence setup .....	30
<b>Figure 3.8</b> Temperature dependent photoluminescence measurement setup.....	31
<b>Figure 4.1</b> Current density-voltage characteristics for 1:5 SiNCs .....	33
<b>Figure 4.2</b> Time-of-flight mobility measurement of SiNCs .....	37
<b>Figure 5.1</b> Steady-state PL spectra and transient PL decays for SiNCs thin film.....	43
<b>Figure 5.2</b> PL emission spectra of SiNCs under pulsed laser excitation .....	44
<b>Figure 5.3</b> Transient PL decay of 1:5 5 nm SiNCs as a function of pump intensity .....	45
<b>Figure 5.4</b> Steady-state PL spectra and energy bandgap of SiNCs at different temperatures.....	46
<b>Figure 5.5</b> PL efficiency of SiNCs at different temperatures .....	48
<b>Figure 5.6</b> Transient photoluminescence decay curve of 3 nm and 5 nm SiNCs .....	49
<b>Figure 5.7</b> Fitted lifetime values of 3 nm and 5 nm SiNCs at different temperatures .....	50
<b>Figure 5.8</b> Calculated exciton decay rates for SiNCs at different temperatures .....	51
<b>Figure 6.1</b> Top view and side view of the interdigitated lateral device .....	55
<b>Figure 6.2</b> Testing geometry of two-tone synchronous spin fraction measurement.....	58
<b>Figure 6.3</b> Energy band diagram of proposed device for spin fraction measurement .....	60
<b>Figure 6.4</b> Schematic plot of thermally activated delayed fluorescence (TADF) .....	61
<b>Figure 6.5</b> Transient decay of 50 mol% m-MTDATA:t-Bu-PBD film .....	62
<b>Figure 6.6</b> Schematic diagram of two energy transfer processes.....	65
<b>Figure 6.7</b> Proposed device structure for PL quenching experiment.....	66
<b>Figure 6.8</b> Comparison of pure FIrpic, pure SiNC and SiNC+FIrpic PL spectra.....	66

# **Chapter 1 Introduction to Semiconductor Nanocrystals**

## **1.1 Introduction**

Nanocrystals (NCs) or quantum dots (QDs) usually refer to tiny crystals consisting of hundreds to a few thousand atoms, with size ranging from 2 to about 20 nm. Typically, when crystal size falls into this regime, quantum mechanical confinement can significantly modify the electronic band structure [1-10]. This opens interesting possibilities to tailor the electrical or optical behavior of a material without changing its chemical composition. For example, by varying the size of NCs, the resulting energy band gap can be easily tuned [3, 11-18].

Inorganic semiconductors are often characterized by superior charge carrier mobilities, photo- and thermal-stability, permitting their integration into high performance electrical and optoelectronic devices [19]. Despite their many attractive features and demonstrated high device performance, device fabrication is often costly due to the use of high temperatures and a difficulty in increasing processing throughput. The latter is complicated in part by the fact that these are often mechanically hard materials that are not compatible with flexible plastic or foil substrates.

Colloidal semiconductor NCs could offer a cost-effective solution to balance the need for high performance with ease-of-processing. Since colloidal NCs form thermodynamically stable solutions, solution-based fabrication process including spin-coating or dip-coating, in addition to conventional large-area coating techniques can be exploited [19-24]. As such, nanomaterials have been recognized as potential building blocks for low cost and large-scale electronic or optoelectronic devices [19, 25-28].

The potential applications for NCs are broad, including photovoltaic cells (PVs) [22, 24, 29-32] and light-emitting devices (LEDs) [21, 33-43]. The tunable electronic band structure [1] and high photoluminescence efficiency [3] makes NCs promising in these areas. In addition, due to their solution processability [44], it is possible to integrate NCs with other novel materials such as organic semiconductors [21, 33-37, 43, 45-49], carbon nanotubes [50-54] or nanowires [55-58] into a hybrid device to further harness the advantage that NCs possess.

## **1.2 Scope of This Thesis**

The main goal of this thesis is to explore the various parameters responsible for the observation of high external quantum efficiency in hybrid silicon nanocrystal-organic light-emitting devices (Si NC-OLEDs). The rest of this chapter is devoted to introducing the basics of nanocrystals, with focus particular focus on silicon nanocrystals (SiNCs). Chapter 2 will discuss the theory and recent progress in NC-OLEDs. Chapter 3 will illustrate the experimental methods used in this thesis. Chapter 4 will discuss the electrical properties of SiNCs, while Chapter 5 will explore the mechanisms for photoluminescence (PL) in SiNCs. Chapter 6 will offer conclusions for this thesis and propose future research directions.

## **1.3 Introduction to Silicon Nanocrystals**

The synthesis of colloidal NCs was first reported in 1993 by Murray et al. [3]. They mixed a hydrophobic solution containing Cd with another that had either S, Se or Te

element at high temperature. Followed with rapid quenching, nanocrystals formed, which would then be quickly passivated by surfactants and became stable in solution. Due to the ease of their chemical synthesis and the excellence of their optical properties (PL efficiency,  $\eta_{PL} \sim 80\%$ ), Group II-VI NCs, such as CdSe [47, 51, 58-65], are considered as the most popular NCs in research.

The research on colloidal SiNCs, however, is less developed as compared with CdSe NCs. This is mainly due to a very low PL efficiency ( $<0.1\%$ ) in the bulk form [66]. Additionally, despite of its good electrical performance, the study of luminescence from Si is complicated by the fact that it is an indirect bandgap material [67]. As a result, the external quantum efficiency of bulk Si based LEDs is typically low.

Silicon nanocrystals (SiNCs) can offer a route around the issues related to the indirect bandgap of silicon. Quantum confinement in SiNCs can supply “momentum conservation” phonons that significantly improve their PL efficiency up to  $\sim 60\%$  [2, 18, 68, 69]. Additionally through precise control on crystal size during the synthesis step [18], tunable emission color by SiNCs could also be experimentally achieved (Figure 1). Additionally, compared with CdSe NCs, SiNCs are considered earth abundant and lower in toxicity, which is desirable for large-scale production. These attributes make SiNCs a promising material for application in LEDs.

Beyond offering a new active material for semiconductor devices, the study of SiNCs may also benefit the whole semiconductor industry.

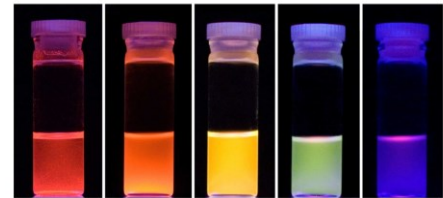


**Figure 1.1** Photographs of deep red (740 nm), red (675 nm), yellow (592 nm), green (572 nm) and blue (441 nm) photoluminescence from SiNCs, pumped at a wavelength of 365 nm. (Reprinted from [18])

Currently, electronic circuits in 22 nm channel length have already been used for commercial applications, with 14 nm technologies under development in laboratories [70]. Due to similarities in feature size, knowledge obtained from studying colloidal SiNCs could help in understanding design rules for next generation electronic circuits.

## 1.4 Quantum Confinement in Nanocrystals

### 1.4.1 Introduction to Quantum Confinement Effect

Size dependent quantum confinement effects begin to modify the bandgap of NCs when their size reaches a critical value, or Bohr radius, which is defined as [71]:

$$a_B = \epsilon_r \frac{m}{m^*} a_0 \quad (1.1)$$

where  $\epsilon_r$  is the dielectric constant of the NC,  $m^*$  is the effective mass of the electron in the NC,  $m$  is the electron rest mass, and  $a_0$  is the Bohr radius of the Hydrogen atom. For CdSe and Si, the Bohr radius are  $\sim 60 \text{ \AA}$  [71] and  $\sim 50 \text{ \AA}$  [72, 73], respectively.

When the NC size falls below its Bohr radius, an exciton, or a bounded electron-hole pair, will experience quantum confinement by the physical crystal boundaries. This will also force the energy bands to split into discrete levels, resulting in a quantized distribution in density of states (the number of states per energy interval per volume that could be occupied by electrons or holes), as shown in Figure 1.2 [67, 74, 75].

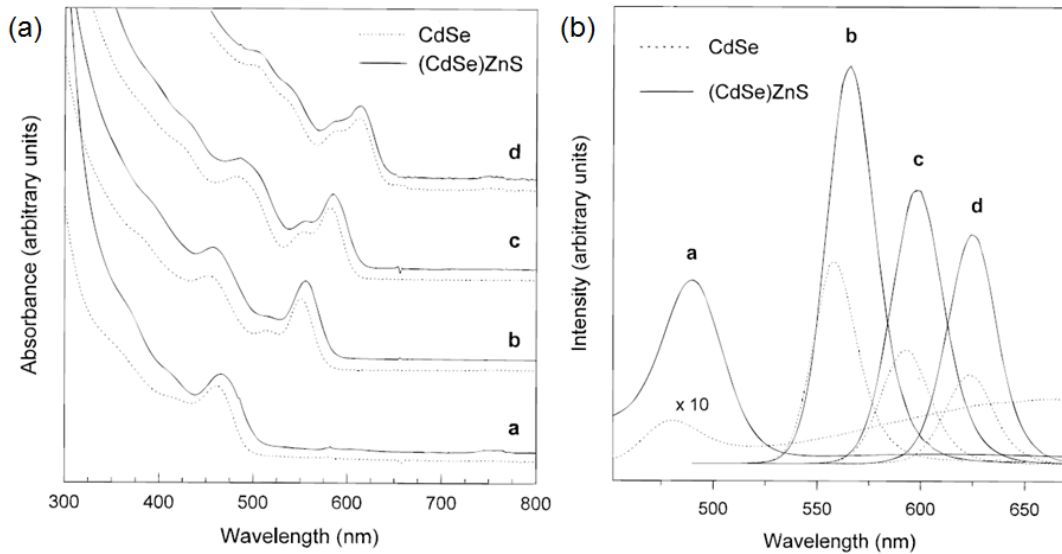


**Figure 1.2** Room temperature size-dependent absorption **(a)** and photoluminescence **(b)** spectra of CdSe NCs (dashed line) and Zinc Sulfide (ZnS) coated CdSe NCs (solid line). The curve **a** refers to particles with average diameter 23 Å, curve **b**: 42 Å, curve **c**: 48 Å, and curve **d**: 55 Å. (Reprinted from [65])

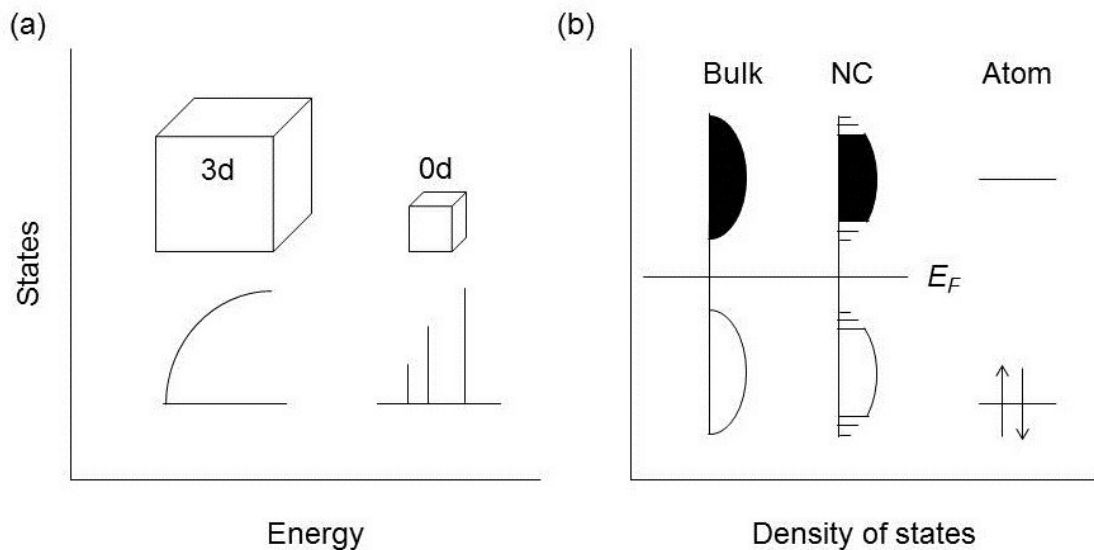


**Figure 1.3** Density of states of a semiconductor: **(a)** Comparison of idealized density of states for one band of a semiconductor in 3-dimensions (3d) and in 0-dimension (0d), with 3d bulk materials showing a continuous density of states and 0d case show a molecular-like (or discrete) density of states; **(b)** The change of density of states from bulk to nanocrystal, and then to atomic limit. Note that the energy band gap between the valence band (VB) and conduction band (CB) increases with decreasing size in the material. The open region and solid region stands for occupied and unoccupied states, respectively.  $E_F$  represents the level of Fermi energy.

### 1.4.2 Quantum Mechanical Model of Confinement

For simplicity, the quantum confinement of a single carrier is often described by the particle-in-a-box model, in which the motion of the electron (or hole) is given by Schrödinger's equation:

$$H\psi = E\psi \quad (1.2)$$

where  $H$  is Hamiltonian operator,  $\psi$  is the wavefunction and  $E$  is the energy of the carrier. Taking the effective mass approximation proposed by Brus [1], the Hamiltonian of a single-charge spherical nanoparticle with a radius  $R$  and with infinite external potential barrier can be written as following:

$$H = \frac{\hbar^2}{8\pi^2 m^*} \nabla_r^2 + V, \quad V=0 \text{ when } r < R \text{ and } V=\infty \text{ when } r \geq R \quad (1.3)$$

where  $\hbar$  is Planck's constant and  $r$  is the distance from the center of the particle. The solution to Equation (1.3) gives:

$$\psi_n(r) = \frac{1}{r\sqrt{2\pi R}} \sin\left(\frac{n\pi r}{R}\right) \quad (1.4)$$

$$E_n = \frac{\hbar^2 n^2}{8m^* R^2} \quad (1.5)$$

Equations (1.4) and (1.5) reveal the behavior of an electron within an infinite potential barrier and also qualitatively describe the observed blue shift in bandgap with shrinking size.

In an excited nanocrystal where both electron and hole exist, the analytical form of  $H$  becomes complicated. In addition to the kinetic energy term, the Coulomb interaction between the electron and hole ( $V_c$ ), and polarization at the NC surface ( $V_p$ ) should also be taken into account [76]. The expression for  $H$  is modified as:

$$H = \frac{\hbar^2}{8\pi^2 m_e} \nabla_e^2 + \frac{\hbar^2}{8\pi^2 m_h} \nabla_h^2 + V_c + V_p \quad (1.7)$$

In which:

$$V_c = -\frac{e^2}{4\pi\epsilon_1|\vec{r}_e-\vec{r}_h|} \quad (1.8)$$

$$V_p = \frac{e^2}{2} \sum_{n=1}^{\infty} \alpha_n \frac{(|\vec{r}_e|)^{2n} + (|\vec{r}_h|)^{2n}}{R^{2n+1}} \quad (1.9)$$

$$\alpha_n = \frac{\left(\frac{\epsilon_1}{\epsilon_2}-1\right)(n+1)}{\epsilon_1\left(\frac{n\epsilon_1}{\epsilon_2}+n+1\right)} \quad (1.10)$$

Here e and h stand for electron and hole, respectively.  $V_c$  and  $V_p$  are both functions of electron and hole position ( $r_e$  and  $r_h$ , refer to Figure 1.4) and  $\epsilon_1$  and  $\epsilon_2$  is the dielectric constant of the NC and the surrounding medium, respectively. Assuming that the electron and hole wavefunctions are uncorrelated, and that the radius  $R$  is small, the solution to Equation (1.2) is:

$$E = E_{g,bulk} + E_{ex} \approx E_{g,bulk} + \frac{\hbar^2}{8R^2} \left( \frac{1}{m_e} + \frac{1}{m_h} \right) \quad (1.11)$$

The sum of the kinetic energy of the electron and hole is approximately taken as the internal energy of the exciton, which adds up to the total energy bandgap of a semiconductor material. From Equation (1.11), the smaller the nanocrystal radius  $R$ , the larger the bandgap, as shown in Figure 1.3, when  $R$  decreases toward the atomic limit. The experimental observed bandgap reveals a good match with the approximation from Equation (1.11) when the size of nanocrystal is greater than 8 nm, as shown in Figure 1.5.

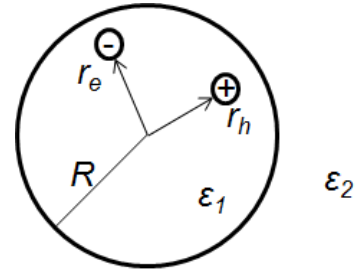


**Figure 1.4** Schematic of a spherical NC with dielectric constant  $\epsilon_1$  embedded in a material with dielectric constant  $\epsilon_2$ .

## 1.5 Charge Carrier Transport in Nanocrystals

Charge injection in semiconductors often depends on the Fermi energy difference between the semiconductor and an injecting metal contact. Ohmic contact for electron transport requires that the Fermi energy (work function) of metal be smaller than the Fermi energy of the

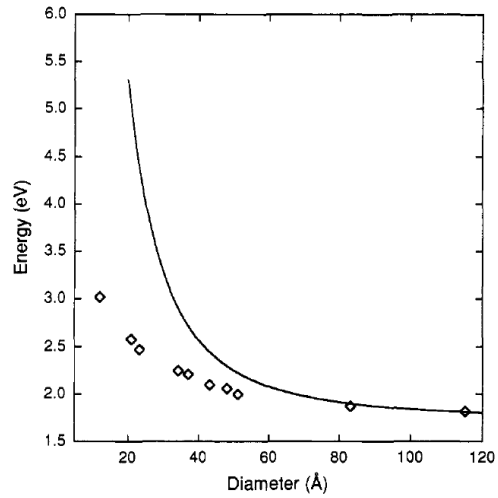


**Figure 1.5** Comparison of the calculated value of the bandgap using the effective mass approximation (solid line) to experimental data (open diamonds) for CdSe NCs. (Reprinted from [3])

semiconductor, which at the same time, also serves as a Schottky barrier for holes. This effect can be used to separate electron and hole transport. Electron-only and hole-only SiNC devices can be made by referring to the energy band diagram in Figure 1.6, allowing electron mobility ( $\mu_h$ ) and hole mobility ( $\mu_e$ ) to be decoupled. For simplicity, energy band bending in the device is ignored and not plotted in the figure.

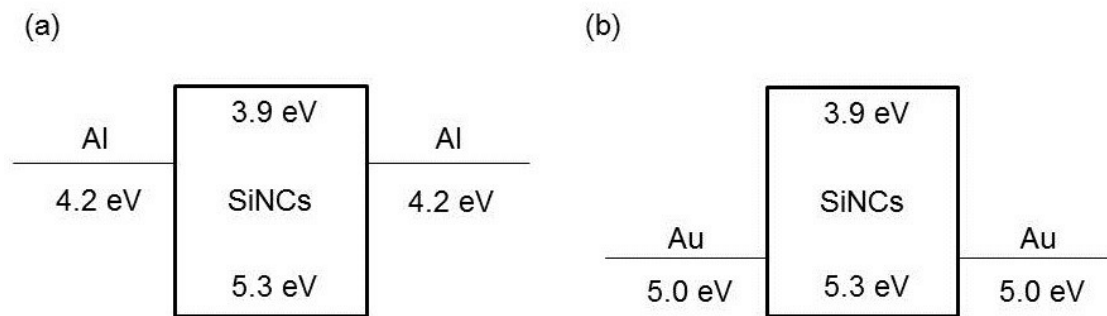


**Figure 1.6** Energy band diagram for (a) an electron only device and (b) a hole only device.

Due to the quantum confinement effect, the valence band (VB) and conduction band (CB) energies for the SiNCs are estimated by correcting those of bulk silicon. The

electroluminescence spectrum of 5 nm SiNCs peaks at  $\sim 868$  nm (1.43 eV) [77], giving a confinement energy  $\sim 0.3$  eV. Of the total confinement energy, 0.2 eV is assigned to the VB, and 0.1 eV is assigned to the CB [14].

Suppose the electron and hole densities are  $n_e$  and  $n_h$ , respectively, the conductivity  $\sigma$  in SiNCs can be expressed as in Equation (1.12).

$$\sigma = n_e e \mu_e + n_h e \mu_h \quad (1.12)$$

Take electron transport as an example. Electrons in excess of thermal equilibrium density  $n_e$  can be injected through Ohmic cathode when the carrier transient time is less than the field-free dielectric relaxation time [78]. This can be viewed as a threshold voltage above which the injected electron density  $n$  exceeds  $n_e$ . This threshold is given by Equation (1.13), where  $e$  is elementary charge,  $d$  is the device thickness and  $\varepsilon$  is the dielectric constant of the semiconductor:

$$V_i = \frac{n_e e d^2}{2\varepsilon} \quad (1.13)$$

Below  $V_i$ , the current density  $J_\Omega$  follows Ohm's law and is linearly proportional to voltage  $V$ , as shown in Equation (1.14). While above  $V_i$ , if there is no trap present,  $J_C$  is limited by the space-charge of injected electrons and follows Equation (1.15) (Mott-Gurney law). This regime ( $J \propto V^2$ ) is often known as space-charge limited conduction (SCLC).

$$J_\Omega = n_e e \mu_e \frac{V}{d} \quad (1.14)$$

$$J_C = \frac{9}{8} \mu_e \varepsilon \frac{V^2}{d^3} \quad (1.15)$$

If traps are present, most of the injected electrons will be localized and not contribute to current flow. This situation applies when  $n_e < n < n_t$ , where  $n_t$  is the trap density. Assuming

the trap energies are energetically exponentially distributed in the band gap, the density of traps per unit energy  $n_t(E)$  will follow Equation (1.16), in which  $N_c$  and  $E_c$  are the density of states and energy of conduction band,  $k_B$  is the Boltzmann's constant and  $T_t$  is the characteristic temperature of traps. The current density  $J_t$  in this regime is found to be proportional to  $V^{l+1}$ , where  $l=T/T_t$ , as shown in Equation (1.17).

$$n_t(E) = \frac{n_t}{k_B T} \exp\left(\frac{E-E_c}{k_B T}\right) \quad (1.16)$$

$$J_t = N_c \mu_e e^{1-l} \left(\frac{e l}{n_t(l+1)}\right)^l \left(\frac{2l}{l+1}\right)^{l+1} \frac{V^{l+1}}{d^{2l+1}} \quad (1.17)$$

For instance, for CdSe NC thin film samples [59], the current has a linear dependence on voltage at low field. As the injected current increases, trap-limited space charge conduction takes place. The transition voltage  $V_\Omega$  is given by Equation (1.18) and indicated by the arrow in Figure 1.7. When  $n$  is further increased to be greater than  $n_t$ ,  $J$ - $V$  relation will fall back to  $V^2$  dependence and enter SCLC regime, illustrated by the top region of the 30 nm sample in Figure 1.7. The transition voltage  $V_c$  between these two regimes is given by Equation (1.19).

$$V_\Omega \approx \left[\frac{n_e}{N_c}\right]^{\frac{1}{l}} \left[\frac{e n_t d^2}{\epsilon}\right]^{l+1} \quad (1.18)$$

$$V_c \approx \frac{e d^2}{\epsilon} \left[\frac{9}{8} \frac{n_t^l}{N_c} \left(\frac{l+1}{l}\right)^l \left(\frac{l+1}{2l+1}\right)^{l+1}\right]^{\frac{1}{l-1}} \quad (1.19)$$

In disordered systems (for example, NC thin films), a field dependent mobility is often observed due to a drop in the potential barrier height  $\Delta U$  for conduction when an electrical field  $F$  is present. Assuming the semiconductor simply is a system of neutral atoms, the potential change when an electron is ionized to a distance  $r$  from nucleus can be thought as the combination of Coulomb force from nucleus and from electrical field,

as shown in Equation (1.20) [79]. The maximum of  $\Delta U$  is found when these two terms equal, which gives the expression in Equation (1.21). Conduction is simply considered as a thermally activated process, thus the expression for mobility can be written as in Equation (1.22), where  $\mu_0$  is zero field mobility and  $\alpha$  (Equation (1.23)) is

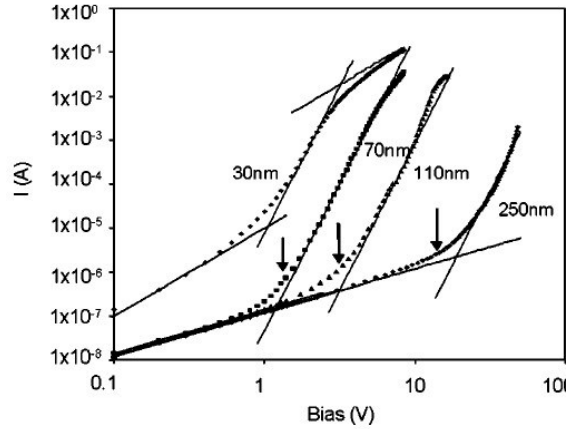


**Figure 1.7** Current-voltage characteristics for CdSe NC devices with a variable thickness of CdSe. Solid lines are fits to the theoretical models. Arrows indicate calculated values for  $V_{\Omega}$ . (Reprinted from [59])

named as Poole-Frenkel coefficient. Taking this field-dependent mobility into account, we can have Equation (1.24) for the current density  $J_{\Omega}$  in Ohmic regime.

$$\Delta U = eFr + \frac{e^2}{4\pi\epsilon r} \quad (1.20)$$

$$\Delta U_m = \sqrt{\frac{e^3 F}{\pi\epsilon}} \quad (1.21)$$

$$\mu(F) = \mu_0 \exp\left(-\frac{\Delta U_m}{k_B T}\right) = \mu_0 \exp(-\alpha\sqrt{F}) \quad (1.22)$$

$$\alpha = \frac{e}{k_B T} \sqrt{\frac{e}{\pi\epsilon}} \quad (1.23)$$

$$J_{\Omega} = n_e e \mu_0 F \exp(-\alpha\sqrt{F}) \quad (1.24)$$

These equations allow us to calculate the mobilities of electron and hole through  $J$ - $V$  measurement. Further discussions will be included in Chapter 4.

## 1.6 Exciton Generation and Recombination in Nanocrystals

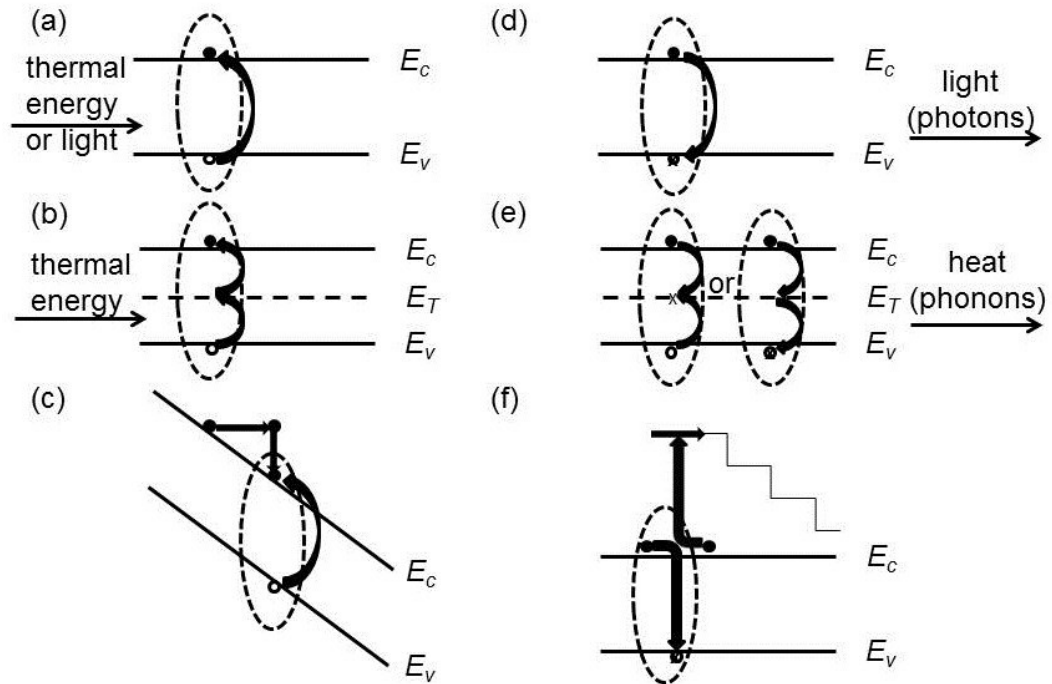


**Figure 1.8** Visualization of generation events via **(a)** band-to-band **(b)** R-G center **(c)** impact ionization processes and recombination events via **(d)** band-to-band **(e)** R-G center **(f)** Auger processes. Solid dot and open dot represent electrons and holes, respectively. Dashed ellipses represent excitons.  $E_c$  and  $E_v$  stand for the energy of conduction band (CB) and valence band (VB).  $E_T$  corresponds to mid-gap trap energy level. x marks a recombination event.

A schematic plot of exciton generation and recombination processes is shown in Figure 1.8. In a bulk semiconductor, an exciton can be formed via: (a) band-to-band generation, in which either thermal energy or light is absorbed to promote an electron from the VB to the CB; (b) Recombination-Generation (R-G) center generation (also referred as Shockley-Read-Hall (SRH) generation), in which thermally assisted generation with an R-G center acting as an intermediary; or (c) impact ionization, which requires a very high electrical field. The recombination process can be thought as the reverse of generation process: (d) band-to-band recombination may lead to photon

emission; (e) R-G center recombination (also referred as SRH recombination), on the other hand, is non-radiative and thus only heat (or phonon) is emitted; (f) Auger processes, which involve two particles (an exciton with a charge carrier, or sometimes two excitons), become

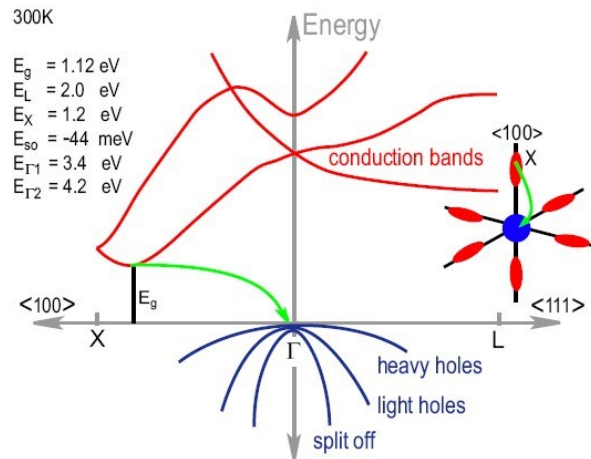


**Figure 1.9** Room temperature energy band diagram of bulk Si. (Reprinted from [39])

likely only when the exciton concentration is high.

In bulk Si, an indirect bandgap semiconductor, radiative band-to-band recombination is ineffective at room temperature. To have band-to-band recombination, a phonon must accompany the process to conserve the crystal momentum. This process is shown by the arrow in the energy band diagram of Si in Figure 1.9. As a result, nonradiative R-G recombination dominates the recombination process in bulk Si [80] and the  $\eta_{PL}$  is very low.

In SiNCs, however,  $\eta_{PL}$  can increase over orders of magnitude relative to bulk Si [18]. The definition of  $\eta_{PL}$  is shown in Equation (1.25), in which  $k_r$  (or  $1/\tau_r$ ) is radiative recombination rate and  $k_{nr}$  (or  $1/\tau_{nr}$ ) is the nonradiative recombination rate. The total decay rate  $k$  (or  $1/\tau$ ) can be easily calculated using the sum of these two terms, as shown in Equation (1.26).

$$\eta_{PL} = \frac{k_r}{k_r + k_{nr}} \quad (1.25)$$

$$k = k_r + k_{nr} \quad (1.26)$$

The increase in  $\eta_{PL}$  in SiNCs compared to the bulk must come either from a decrease in  $k_{nr}$  and/or an increase in  $k_r$ . The former is likely due to the decrease of R-G centers, which dominate the non-radiative recombination process in bulk Si [80]. In nanocrystals that are small enough to show quantum confinement effects, as some authors argued [39], the R-G centers (midgap defects) are thermodynamically unfavorable and tend to grow out of the nanocrystal.

There are two factors that contribute to improvement in the radiative recombination rate  $k_r$ . First, the uncertainty in momentum space that quantum confinement introduces relaxes the momentum conservation rule and allows a greater proportion of the phonon to assist in the indirect band-to-band transition [81]. This effect is thought to be insufficient to make the bandgap of SiNCs direct but the optical transitions might possibly be described as less indirect or quasi-direct [68]. Second, because the nanocrystal forms a potential well that confines the electron and the hole spatially, their wavefunctions overlap more in position space, recombination events between electrons and holes become more likely to occur [2].

In most cases, exciton decay is characterized by Equation (1.27), where  $g$  is the exciton generation rate and  $n$  is the exciton concentration. When a pulsed laser source ( $< 1$  ns in pulse width) is used,  $g$  becomes 0 at  $t > 0$ . The solution gives a single exponential decay, as shown in Equation (1.28).

$$\frac{dn}{dt} = g - kn \tag{1.27}$$

$$n(t) = n_o \exp(-kt) \tag{1.28}$$

If excitons are dominated by single exciton decay (without nonlinear terms), the PL intensity  $I$  is linearly proportional to exciton density  $n$ . It should however be noted that the recombination processes in SiNCs are likely more complicated. Surface recombination and Auger recombination, which are ignored in the previous discussion, may be even worse in SiNCs than in bulk. This is due to the higher surface-to-volume ratio and higher exciton concentration within the small nanocrystal volume [82]. In SiNCs, instead, stretched exponential decay fitting (Kohlrausch decay equation), is frequently used (Equation. (1.29)).

$$n(t) = n_0 \exp[-(kt)^\beta] \quad (1.29)$$

In this equation, an empirical fitting parameter  $\beta$ , sometimes named as dispersion coefficient, is used to explain the discrepancy from single exponential fitting (where  $\beta=1$ ). The dispersion coefficient  $\beta$  is usually explained by lifetime distribution due to size variation in NCs [83] or exciton transfer between NCs [84]. To better understand the decay dynamics of excitons and the origin of photoluminescence in SiNCs, further study is thus needed. This will be discussed in detail in Chapter 5 in the thesis.

# Chapter 2 Introduction to Hybrid Nanocrystal-Organic Light-Emitting Devices

## 2.1 Introduction

Light-emitting-device (LED) has emerged as a potential approach to save energy and alleviate global warming [85]. In such devices, the conversion efficiency from electricity to light emission is 5~6 times higher than incandescent light bulbs [85]. In addition, LEDs are also considered as longer in working lifetime, and lower in maintenance requirement. These attributes of LEDs could lead to a complete revolution in the lighting industry in the near future.

In history, LEDs were discovered more than 100 years ago [86]. Until recently, most research has focused on inorganic semiconductor LEDs, with the study of organic LEDs (OLEDs) only beginning in 1987 [87]. Recently, hybrid-material based LEDs, such as hybrid nanocrystal-organic light-emitting devices (NC-OLEDs) have gained in their interest due to the ease that the LED emission wavelength can be tuned through variations in NC size.

The first NC-OLED was demonstrated in 1994 using group II-VI CdSe NCs, and a conjugated polymer, poly-(para-phenylenevinylene) (PPV) [43]. Although the external quantum efficiency ( $\eta_{EQE}$ , photons out per electron in) of this device was only 0.001% [43], this work sparked new interest in the area of hybrid optoelectronic devices. To date, most work has focused on compound semiconductor NCs including group II-VI [21, 35, 43, 65, 88, 89], III-V [41], and IV-VI [49, 90]. Core-shell structured Group II-VI NCs were also utilized to help increase the device efficiency. Very recently, an impressive

external quantum efficiency of 18% was reported using CdSe/CdS (core/shell) NCs [35]. This was the first time for a hybrid NC-OLED reported with efficiency comparable to that of phosphorescent OLEDs [91]. In Table 2.1 progresses made in the last two decades on NC-OLEDs are briefly summarized.

Nanocrystals	Emission Wavelength	External Quantum Efficiency	Turn-on Voltage	Year
CdSe	580-620 nm	0.001-0.01%	~4 V	1994
CdSe/CdS	613 nm	0.22%	~4 V	1997
CdSe/ZnS	562 nm	0.52%	~4 V	2002
CdSe/ZnS	540-635 nm	>2%	-	2005
CdSe/ZnS	600 nm	2.7%	~2.5 V	2009
CdSe/ZnS	~610 nm	18%	~1.7 V	2013

**Table 2.1** Summary of the progress of NC-OLEDs in the visible emission range.

In addition to displays and solid-state lighting in the visible spectrum, NCs also have the potential to be applied to the near infrared (NIR) and infrared for application in optical communications (1300 nm - 1500 nm) [15, 49, 90] and tissue imaging (800 nm - 1100 nm) [92-94]. CdSe NCs, due to the large bulk energy bandgap (1.74 eV, corresponds to ~710 nm), cannot emit in the near infrared spectrum. The tunability of frequently-seen semiconductors is shown in Figure 2.1. From this plot, group III-V [41] and group IV-VI NCs [15, 49, 90] are both good candidates for NIR emission. In fact, due to similarity in colloidal synthesis procedures, research interest in group IV-VI NCs, especially PbS and PbSe NCs has grown in recent years.

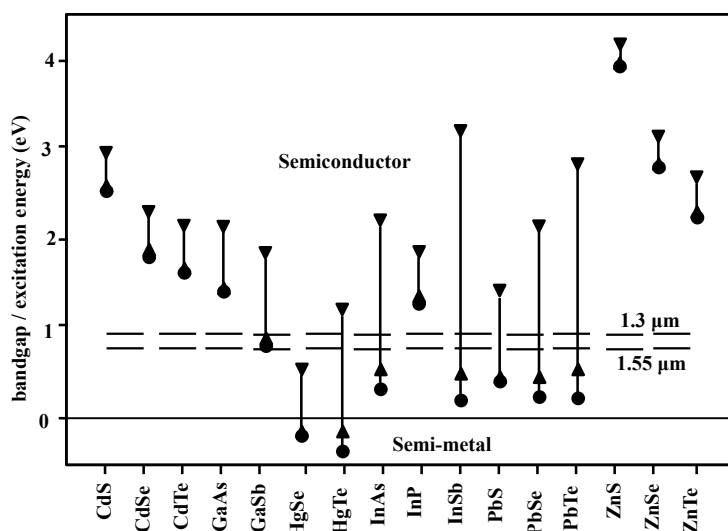


**Figure 2.1** Tunable energy bandgap of NCs. The bandgap energies are calculated using a simple particle-in-a-box model [1]. Circles stand for the bandgap energies of bulk materials. Downward-pointing triangles show energies of 3 nm nanocrystals, and upward-pointing triangles show energies for nanocrystals at 10 nm. The optical communication window (1.3  $\mu\text{m}$  to 1.55  $\mu\text{m}$ ) is also marked as reference. (Reprinted from [44])

In Table 2.2, progress in group III-V and group IV-VI NIR NC-OLEDs is summarized [38, 41, 46, 95]. Unlike visible emitting NC-OLEDs, their external quantum efficiencies are typically lower, with the maximum only at 2% [95]. Despite the slow improvement, the device efficiency still lags the requirements for commercialization. As such, new semiconductor materials are proposed to solve this issue, for instance, SiNCs [77]. This will be discussed in the next session.

Nanocrystals	Emission Wavelength	External Quantum Efficiency	Turn-on Voltage	Year
InAs/ZnSe	1300 nm	0.5%	15 V	2002
PbSe	1495 nm	0.001%	10 V	2003
PbS	1200 nm	1.15%	1 V	2008
PbS	1054 nm	2.0%	1.2 V	2012

**Table 2.2** Summary of reported near-infrared-nanocrystal electroluminescence.

## 2.2 Operating Mechanism of Hybrid SiNC-OLEDs

Electroluminescence (EL) in nanostructured Si, or porous Si, was first discovered in early 1990s [96]. Field-effect EL in SiNCs was later demonstrated in 2005 [40]. Our group showed that a hybrid SiNC-organic LED (NC-OLED) can have an external quantum efficiency ( $\eta_{EQE}$ ) of 0.6% in the NIR [77]. With careful choice of hole-transport material, device efficiency has been improved up to 8.6% [34], a record efficiency for NIR NC-OLEDs.

A typical structure for a SiNC-OLED is shown in Figure 2.2. The SiNC-OLEDs are fabricated by sandwiching the inorganic NC emissive layer (EML) between organic charge transport layers. Detailed procedures can be found in [34]. Briefly,

PEDOT:PSS and poly-TPD solution are spun-coated on clean ITO substrates. Followed with heat and UV treatment to stabilize these layers, SiNCs are then spun-coated on top. Finally, Alq<sub>3</sub> and Al are deposited using thermal evaporation, defining a device contact area of a circle in 1 mm diameter.

The energy band diagram of the Si NC-OLED with optimized efficiency is shown in Figure 2.3. As can be seen in this plot, when the ITO anode is forward biased with respect to the LiF/Al cathode, holes are injected from the ITO and electrons from Al. The

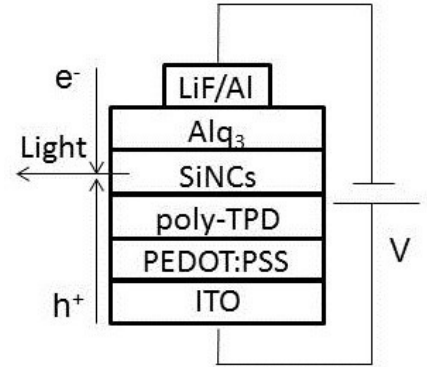


**Figure 2.2** Structure of a hybrid Si NC-OLED. Indium tin oxide (ITO) is used as transparent anode, poly(3,4-ethylenedioxythiophene):poly(styrenesulfonate) (PEDOT:PSS) as an injection layer (HIL), poly(4-butylphenyl-diphenyl-amine) (poly-TPD) as a hole transport layer (HTL), SiNCs as an emissive layer (EML), tris(8-hydroxyquinolino)aluminum (Alq<sub>3</sub>) as an electron transport layer (ETL) and lithium fluoride (LiF)/Al as the cathode.

electrons and holes form excitons that are confined to the SiNC layer, which may then recombine radiatively and emit photons.

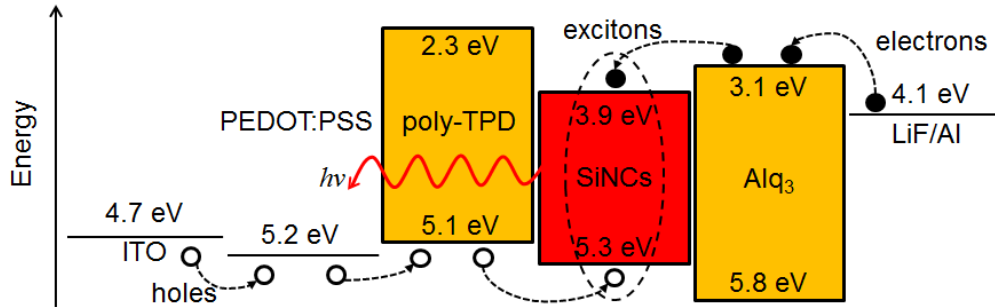


**Figure 2.3** Energy band diagram of a Si NC-OLED, using 5 nm SiNCs. Open dots and solid dots stand for holes and electrons separately.

### 2.3 External Quantum Efficiency of Hybrid SiNC-OLEDs

The external quantum efficiency ( $\eta_{EQE}$ ) is the ratio of forward-emitted photons per injected electron. Formally, the  $\eta_{EQE}$  is defined as:

$$\eta_{EQE} = \eta_{OC} \gamma \chi \eta_{PL} \quad (2.1)$$

where  $\eta_{OC}$  is the optical outcoupling efficiency, which is the fraction of internally generated photons that escape into the forward viewing direction (Figure 2.4). A significant portion of photons are indeed trapped inside the device due to total internal reflection (TIR) and waveguiding in the organic layers or in the substrate. Additionally, photons formed in the organic layer can also be quenched by the metal

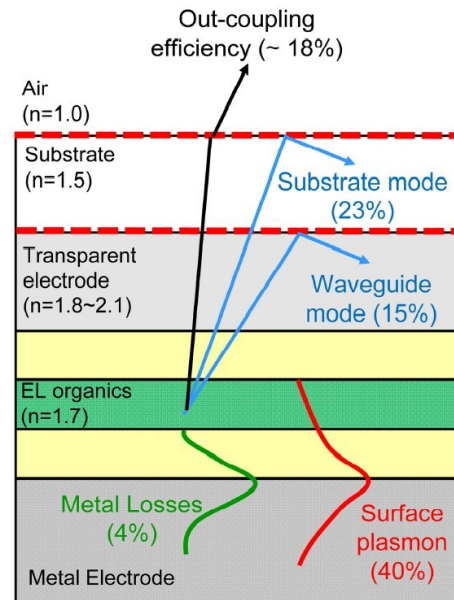


**Figure 2.4** Various kinds of light out-coupling losses in OLEDs. (Reprinted from [97])

electrode. As a result,  $\eta_{OC}$  is typically <20% in OLEDs [97]. It should be noted that as the refractive index of SiNCs ( $n \sim 3.5$  in bulk form) and emission wavelength of SiNC-OLEDs are different from typical organics and OLEDs, the estimation is rough. However, a recently publication shows that infrared emitting PbSe ( $n \sim 16$  in bulk form) NC-OLED has a  $\eta_{OC} \sim 20\%$  at 1150 nm [98]. So for simplicity, we assume  $\eta_{OC}$  as 20% in our SiNC-OLEDs.

The charge balance factor,  $\gamma$ , is the fraction of injected carriers that actually form excitons in the EML. It is difficult to probe  $\gamma$  directly but it is generally believed that in state-of-art, high efficient OLEDs where mobilities of electrons and holes are well balanced and where blocking layers prevent leakage current,  $\gamma$  could reach unity.

The exciton spin fraction  $\chi$  is defined as the ratio of singlet exciton states over the sum of singlet and triplet exciton states. A singlet exciton is formed when a ground state (a pair of electrons, with one spin up and another spin down) is optically excited. To conserve spin momentum, the electron in the excited state will have different spin direction compared to the ground state electron, resulting in net spin  $S=0$  (Figure 2.5 (a)). However, if the exciton is formed via electrical excitation, each electron could have an independent electron spin orientation. This process can be visualized by using the vector model as shown in Figure 2.5, where the electron spin is treated as a rotating vector with an orbital momentum. The individual vectors represent the state of either spin up or spin down. If the two electrons have the same spin direction, a triplet state is formed, with a net spin  $S=1$  (Figure 2.5 (b) to (d)). Simple spin statistics predicts that under electrical excitation there will be three times as many triplet excitons as there are singlet excitons

[99]. As a result, for a fluorescent OLED in which only singlets can radiatively emit, spin fraction  $\chi$  equals 0.25. While in CdSe NCs, it has been argued that  $\chi$  could be close to unity [35], spin statistics remains unclear in SiNCs. It is very unusual for a light atom such as Si to show phosphorescence at room temperature. If SiNCs could only fluoresce, the value of  $\chi$  is also 0.25.

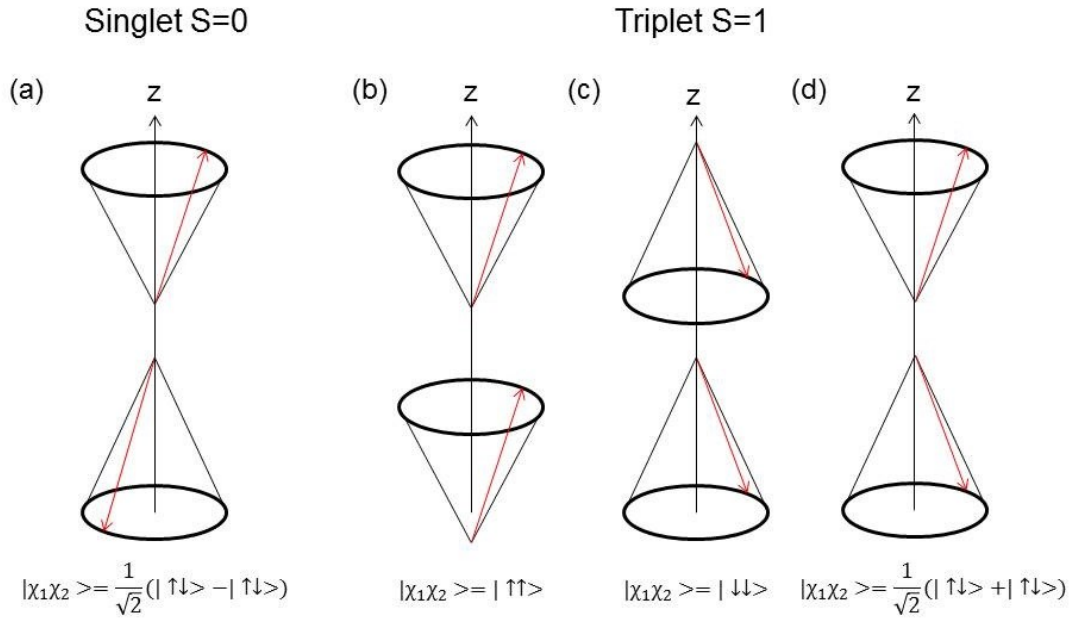


**Figure 2.5** Illustration of four possible exciton spin combinations. **(a)** Singlet S=0; **(b)**, **(c)**, and **(d)** Triplet S=1. (Adapted from [99])

The PL efficiency ( $\eta_{PL}$ ) is the ratio of emitted photons per absorbed photons for a given material. In our experiment, SiNCs typically have a  $\eta_{PL} > 50\%$  in solution. Detailed on the PL efficiency in SiNCs will be covered in Chapter 3 and Chapter 5 in this thesis.

## 2.4 Motivation of This Thesis

Following the discussion in previous section, with  $\eta_{OC}=0.2$ ,  $\gamma=1$ ,  $\chi=0.25$  and  $\eta_{PL}=1$ , the maximal theoretical EQE is calculated only to be 5%. However, it is noted that EQE

in our optimized SiNC-OLEDs is 8.6% (black curve in Figure 2.6). The calculation assumes the other 3 factors at maximum, so the increase in the device efficiency must come from an increase in the spin fraction  $\chi$ . This gives the first motivation of the thesis, to explore the physical origin of high spin fraction in our SiNC-OLED, including measuring the accurate value

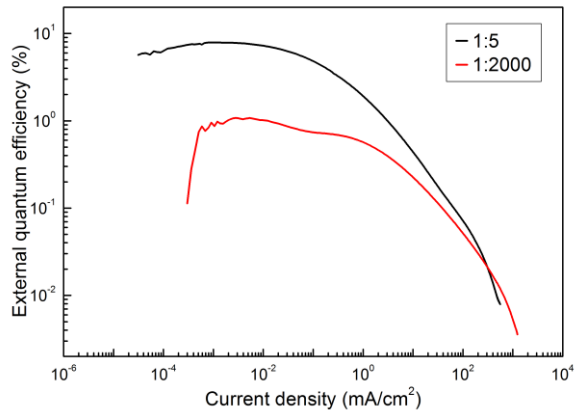


**Figure 2.6** External quantum efficiencies of SiNC-OLEDs made from 1:5 (black) and 1:2000 (red) SiNCs. The ratio denotes the amount of ligand to solvent added during the functionalization step. (Data courtesy by Dr. Kai-Yuan Cheng)

for the spin fraction from experiment and determining possible mechanisms to explain it.

As also can be seen from Figure 2.6, SiNCs passivated with different amount of ligands are used to fabricate device. Interestingly, it is found that less passivated 1:2000 sample (red curve in Figure 2.6) has a much lower efficiency, suggesting a possible difference in either electrical ( $\gamma$ ) or optical properties ( $\eta_{PL}$ ) due to change of passivation. This is another meaningful topic that calls upon our attention. Could we further improve the efficiency of the SiNC-OLED by engineering the surface ligands? To test these ideas, electrical and optical experiments on SiNCs will be conducted in the latter chapters.

To sum the goals of this thesis:

- Explore charge carrier transport (Chapter 4) and photophysics (Chapter 5) in SiNCs with different amounts of surface ligand passivation.
- Explore the physical origin of high spin fraction  $\chi$  in SiNC-OLED. (Chapter 5 and 6)

## Chapter 3 Experimental Procedures

### 3.1 Synthesis and Functionalization of Silicon Nanocrystals

#### 3.1.1 Non-thermal Plasma Synthesis of Silicon Nanocrystals

Details on the non-thermal plasma synthesis of silicon nanocrystals (SiNCs) can be found in [100]. The SiNCs used in this thesis were supplied by Ting Chen in Prof. Uwe Kortshagen's research group at the University of Minnesota. Briefly, in order to prepare 5 nm SiNCs, silane in a mixture of He (5:95) and Ar at 12-14 and 25-30 sccm, respectively, are injected into a 9.5 mm o.d. Pyrex tube and are dissociated with 85-100 W of RF power at 1.4 Torr. The as-produced bare SiNCs formed in the plasma are then collected at the exhaust of the reactor on a stainless steel mesh, as shown in Figure 3.1(a). A transmission electron micrograph (TEM) of bare SiNCs is shown in Figure 3.2.

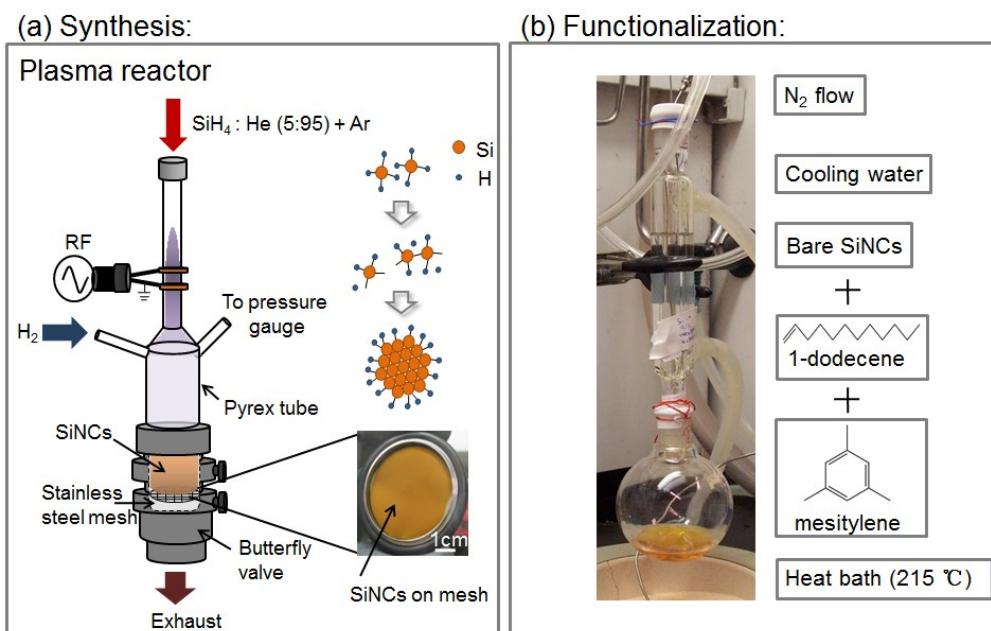


**Figure 3.1** Pictures showing (a) non-thermal plasma synthesis and (b) functionalization of SiNCs. Photographs courtesy of Lorenzo Mangolini in Prof. Uwe Kortshagen's group.

The as-produced SiNCs, which are not passivated, only have a PL efficiency of ~10% in solution, which can be further enhanced [100]. One main reason for it is that the as-produced SiNCs are quickly oxidized when exposed to air. To prevent that, surface functionalization is thus required. More importantly, surface functionalization could also increase the solubility of SiNCs in non-polar solvents, which could be very useful in solution-based manufacture.

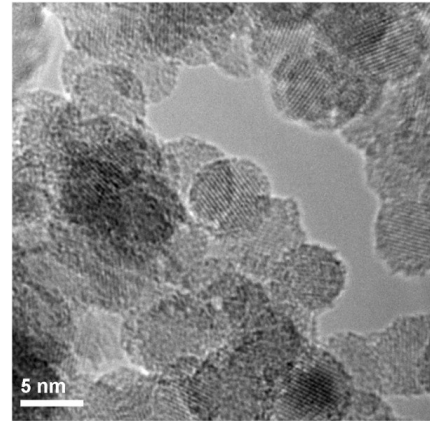


**Figure 3.2** Transmission electron micrograph of silicon nanocrystals (SiNCs) synthesized in non-thermal plasma process. Picture courtesy by Lorenzo Mangolini in Prof. Kortshagen's group.

### 3.1.2 Functionalization of Silicon Nanocrystals

Surface passivation of the SiNCs is performed by dissolving the particles in a solution mixture of mesitylene and 1-dodecene and boiling at 205°C for 2-3 hours under reflux conditions, as shown in Figure 3.1 (b). After the functionalization step, the SiNCs are surface-terminated with Si-C covalent bonds [101], following the hydrosilylation reaction shown in Figure 3.3.

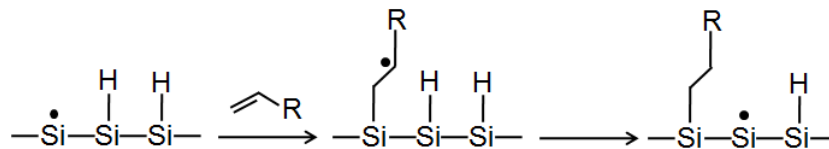


**Figure 3.3** Proposed functionalization mechanism in SiNCs [101].

In our experiments, different amount of surface ligand coverage on SiNCs are achieved by changing the volume ratio of 1-dodecene over mesitylene in the

hydrosilylation solution. Here, we use 1:5, 1:1000 and 1:2000 to denote the volume ratio of these two. A rough estimation shows that for the 1:5 sample, ideally almost all the surface atoms on the SiNCs are passivated with ligands; while in 1:1000 sample, only half of the surface atoms are covered, as shown in Table 3.1.

Ratio of ligands v.s. solvent (mL/mL)	1:5	1:1000	1:2000
1-dodecene (mL)	6.7	0.04	0.02
Number of ligands	$1.91 \times 10^{22}$	$1.15 \times 10^{20}$	$5.73 \times 10^{19}$
Ratio of ligands/particle	74609	449	224
Surface atoms/particle	909	909	909
Surface atom capping ratio	100%	49%	25%

**Table 3.1** Surface SiNC atom capping ratio, calculated for adding 20 mg SiNCs into 40 mL hydrosilylation solution. Here it is assumed that all the ligands added can attach to the surface atom and each surface atom can only be in connection with a single ligand. Table courtesy by Ting Chen in Prof. Kortshagen's group.

## 3.2 Electrical Characterization

### 3.2.1 Current-Voltage Measurements

The devices used for current density-voltage ( $J$ - $V$ ) measurements are prepared following the scheme in Figure 1.6. Device substrates are first rinsed with Tergitol (from Sigma-Aldrich) and deionized water and sonicated for 5 min. Samples are then twice sonicated in acetone for 5 min. Finally, boiling isopropanol is used to clean residual organics off the substrate. The clean glass substrates are then dried with nitrogen gas and immediately put inside an Angstrom Engineering vacuum chamber for thermal evaporation of the bottom contact layer, either Al or Au. The SiNC solution (with a concentration of 20 mg/mL in chloroform) is then spun-coated on top of the bottom contact layer at different conditions. Finally, the device is thermally evaporated with top

metal contact again using a shadow mask, defining a device contact area of a circle in 1 mm diameter. All these steps are conducted in a nitrogen glove box.

Current density-voltage measurements are conducted in air ambient. A gold wire with a diameter of 25  $\mu\text{m}$  is used to make top contact without damaging the device and a hard tungsten probe is used for bottom contact. The experimental data was collected by an Agilent semiconductor parameter analyzer 4155C. Device thickness is measured using tapping mode in a scanning probe microscopy (SPM). We scratch a trench on the SiNCs thin film using a razor blade and take the average height difference between the scratched and unscratched regions as the film thickness. Care must be taken to reduce the possible damage on the glass substrate by the blade. A typical thickness scan on SiNCs thin film is shown in Figure 3.4.

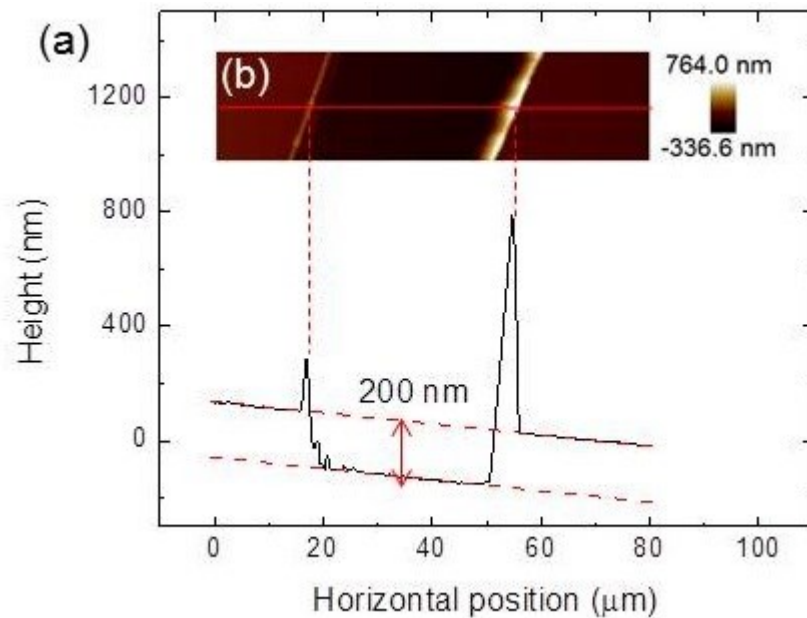


**Figure 3.4** (a) Thickness versus horizontal position profile of the red solid line in the SPM image (inset (b)) of an Al/SiNC/Al device. The boundary of the trench is marked with red dashed lines. As the bottom contact Al electrode has a thickness of 100 nm, the real thickness of SiNC thin film is 100 nm.

### 3.2.2 Time-of-Flight Mobility Measurements

The device architecture used for time-of-flight (TOF) measurements is made on patterned ITO substrates. A schematic of the device is shown in Figure 3.5 (a), with a larger device area (3 mm by 3 mm). As in this experiment, the device is held vertically with large voltage bias applied, alligator clips are used to make electrical contact in replace of tungsten probes and gold wires.

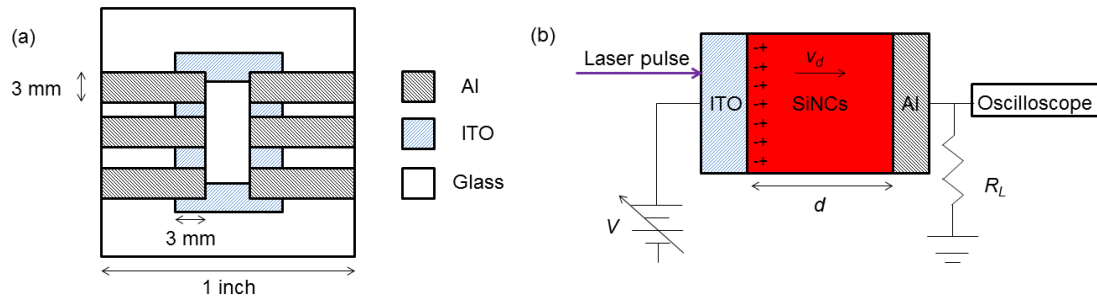


**Figure 3.5 (a)** Schematic patterned ITO substrate and **(b)** Experiment setup for mobility measurement of SiNCs using time-of-flight.  $V$  is the applied voltage on the SiNCs thin film and  $d$  is the film thickness.  $R_L$  is the load resistance and  $v_d$  is the speed of charge carrier.

In the experiment setup (Figure 3.5 (b)), a pulsed  $N_2$  laser from Optical Building Blocks (337 nm in central wavelength and 800 ps in pulse width) pumps excitons in the SiNCs thin film and the generated excitons are quickly dissociated into charge carriers and then swept out by a strong applied electrical field ( $\sim 10^6$  V/cm). A Sorensen DC power supply (XHR600-1.7) is used as the voltage source and a Tektronix oscilloscope (TDS2004B) is used to measure the voltage change across the external load resistance to determine the amount of generated photocurrent. Neutral density filters and concentration lenses were used to focus the laser beam spot on the device under test at moderate illumination intensity. The hole mobility  $\mu_h$  is measured by positively biasing ITO with respect to Al, and the reverse configuration can be used to probe electron mobility  $\mu_e$ .

### 3.3 Optical Characterization

#### 3.3.1 Room Temperature Steady-state Photoluminescence

In order to characterize SiNC PL, SiNCs were spun-cast onto clean glass or silicon (with native oxide) substrates, followed by baking on a hotplate at 64°C for 1 hour. Clean glass substrates are first put inside an integration sphere as a reference, under illumination at 385 nm (Hg lamp) (Figure 3.6 (a)). The SiNCs thin film sample is also put inside the same integration sphere to measure the change in the spectrum, as shown in Figure 3.6 (b). The spectral change around 385 nm is due to the absorption of SiNCs (black curve), while the change at infrared wavelength is due to their photoluminescence emission (red curve). The PL efficiency is obtained by dividing the integrated area of the emission curve over the area of absorption curve.

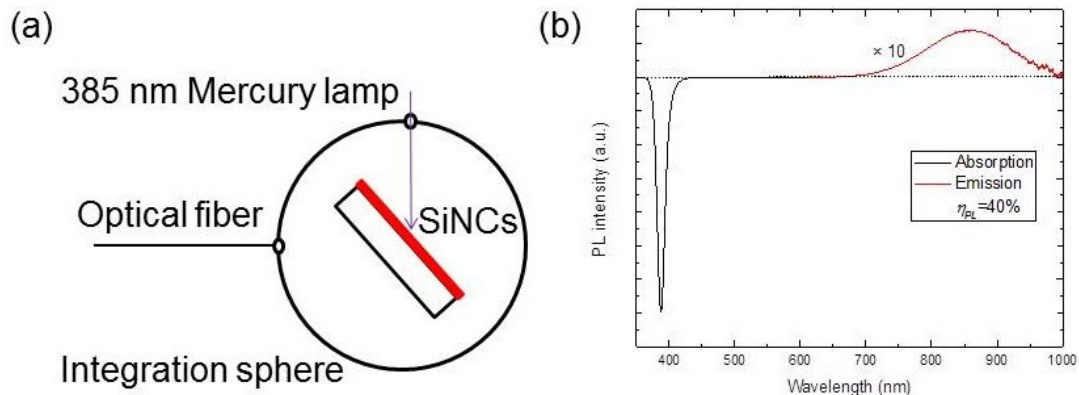


**Figure 3.6 (a)** Room temperature photoluminescence efficiency measurement setup. **(b)** Absorption and emission spectra of a 1:5.5 nm SiNC thin film sample.

A spectrometer (HR-USB2000) coupled to an optical fiber (from Ocean Optics, with a diameter of 1 mm) is used to capture the optical signal. In this experiment, an

integration time of 115 ms and an average of 50 times are applied.

### 3.3.2 Room Temperature Transient Photoluminescence

For measurements of transient PL, a small area photodetector with a diameter of 1 mm (PDA-10A from Thorlabs), coupled to an oscilloscope (Tektronix TDS2004B, with both 50  $\Omega$  and 1M $\Omega$  input) is used. The experiment setup is shown in Figure 3.7. A low-pass colored glass filter (450 nm, from Edmund Optics) is used to cut off the incident laser beam. An average of 100 scans is used in this experiment.

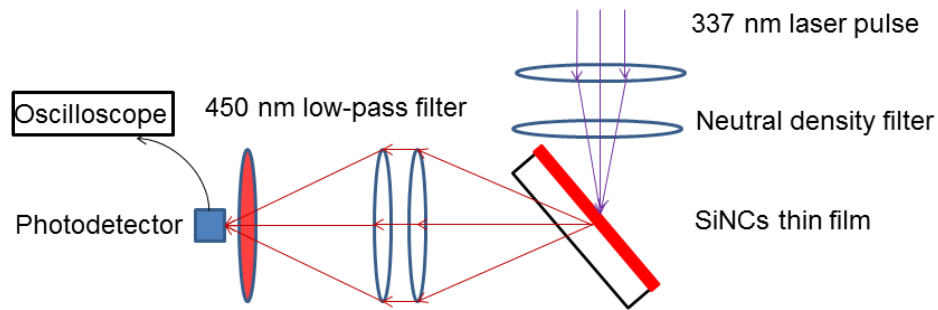


**Figure 3.7** Room temperature transient photoluminescence testing setup.

### 3.3.3 Temperature Dependent Steady-state and Transient Photoluminescence

This experiment is conducted with a liquid nitrogen cryostat (VPF-100 from Janis) and the setup is shown in Figure 3.8. A Lakeshore 325 temperature controller with 2 thermal couples is used to change the temperature on the substrate from room temperature (296 K) to 78 K. A mechanical rough pump is also used to decrease the pressure inside the cryostat to 2.0 mTorr to reduce potential heat exchange to the room

ambient. Different from steady-state room temperature PL efficiency measurement, a 405 nm semiconductor laser with a power of 60 mW and spot size of 1 mm by 2 mm is used as the light source. In this case, the PL signal collection is limited by the geometry of the cryostat. So a longer integration time (1s) with 5 average times are used to increase the number of photons captured. The same setup is also used for capturing transient PL signal, but with PDA-10A photodetector in replace of using an optical fiber.

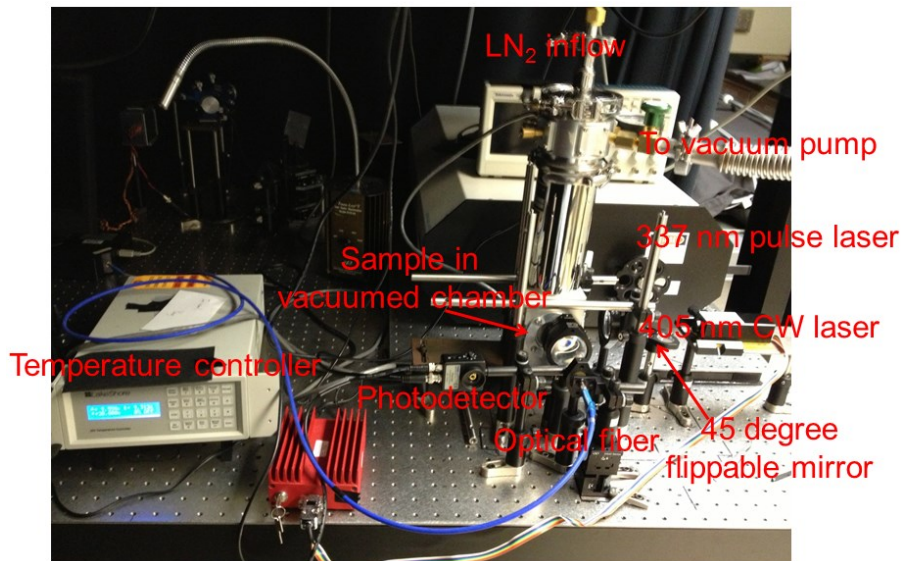


**Figure 3.8** Temperature dependent photoluminescence measurement setup.

## **Chapter 4 Charge Transport in Silicon Nanocrystals**

### **4.1 Foreword**

As discussed in section 2.5, the external quantum efficiency of Si NC-OLEDs decreases significantly for less-passivated SiNCs. One possible reason is due to a decrease in the charge balance factor  $\gamma$ , or imbalance in charge carrier mobilities in SiNCs. So in this chapter, the electrical conductivity and mobility will be measured to explore the relationship between degree of passivation and charge transport in SiNCs.

Charge transport has been well studied in inorganic semiconductor nanocrystals [23, 59, 102-106]. However, most of the research is focused on characterizing the charge carrier mobilities using thin film transistors (TFTs) instead of simple  $J$ - $V$  measurement [59]. In addition, chemical treatment [23, 102] and high temperature baking [103, 104] are frequently used on the NC films to reduce interparticle distance and help improve mobility. As we are interested in the intrinsic transport behavior of SiNCs in our SiNC-OLEDs, it is desirable to have them tested in a similar diode configuration without complicated treatment after the NC films are formed. Thus, following the energy band diagram in Figure 1.6, we construct devices (Figure 4.1 (b)) to probe the electrical properties in SiNCs.

### **4.2 Electrical Conductivity in Silicon Nanocrystals**

We start with characterization of electron transport in SiNCs, using Al contacted device (Figure 4.1 (b)).

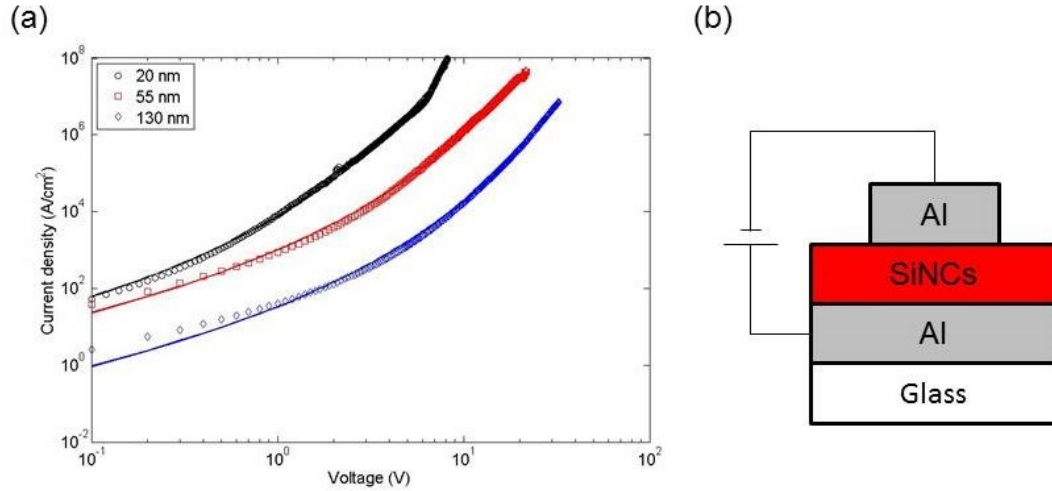


**Figure 4.1** (a) Current density-voltage characteristics for 1:5 SiNCs as a function of film thickness ( $\circ$ :20 nm,  $\square$ : 55 nm,  $\diamond$ :130 nm) in a vertical device structure. Solid lines are fits. (b) Device structure for electron conductivity measurements. The device top contact has an area of a circle in 1 mm diameter.

The  $J$ - $V$  plot can be fit well using Equation (1.24), Ohmic conduction with field-dependent mobility. It is expected that many traps are present in the NC thin film prepared by spin-coating. However, a clear transition point from higher order  $V^{l+1}$  (where  $l+1$  is the slope of  $J$ - $V$  curve in trap-limited SCLC and  $l>1$ ) to  $V^2$  dependence in  $J$ - $V$  curve is not observed, thus the trap-free SCLC model (Equation (1.15)) cannot be applied here. One possible reason is that the current density is relatively high so that the device breaks down before it can reach the SCLC regime. This result differs from previous reports in which either trap-free [107] or trap-limited SCLC [108, 109] is observed in SiNCs. Such difference might come from both NC sizes and surface conditions. The extracted conductivity of the electron ( $\sigma_e$ ) and Poole-Frenkel coefficient  $\alpha$  are listed in Table 4.1.

Thickness (nm)	$\sigma_e$ ( $\Omega^{-1}\text{cm}^{-1}$ )	$\alpha$ ( $\text{cm}^{0.5}\text{V}^{-0.5}$ )
20	$3.66 \times 10^{-8}$	$5.22 \times 10^{-3}$
55	$6.42 \times 10^{-8}$	$5.04 \times 10^{-3}$
130	$6.73 \times 10^{-9}$	$6.71 \times 10^{-3}$

**Table 4.1** Electron conductivity and Poole-Frenkel coefficient for 1:5 SiNCs.

Here we are not able to determine the value for mobility  $\mu_e$  because it is coupled with electron carrier density  $n_e$ . If the intrinsic carrier density in bulk Si  $n_i$  ( $10^{10} \text{ cm}^{-3}$ ) is taken as  $n_e$ , the calculated  $\mu_e$  is on the order of  $10^{-3} \text{ cm}^2\text{V}^{-1}\text{s}^{-1}$ , a very high value for a NC device without any chemical treatment or high temperature treatment. It should be mentioned that in SiNCs where quantum confinement plays a role, both the energy band structure and the value of  $n_i$  change significantly. As a result, this estimation of  $\mu_e$  may be inaccurate. In the 130 nm sample, the lower conductivity value suggests less close-packed film morphology and larger interparticle distance, which might result from a lower spinning rate (800 rpm).

The Poole-Frenkel coefficient  $\alpha$  extracted from the fits is smaller than its theoretical value ( $\alpha_{th}=8.57 \times 10^{-3} \text{ cm}^{0.5}\text{V}^{-0.5}$ ) by using Equation (1.23) and  $\epsilon_r=11.7$  (bulk Si). The deviation in  $\alpha$  can be explained using the model proposed by Hill [110]. In the original model [79] to derive  $\alpha$ , the hole (atom core) is taken as immobile, which in fact it is not always true. Taking this modification into account, the effective Poole-Frenkel coefficient  $\alpha_e$  is given by Equation (4.1), in which  $v_e$  and  $v_h$  are effective velocities of electrons and holes.

$$\alpha_e = \alpha \frac{2v_e - v_h}{2v_e} \approx \alpha \frac{2\mu_e - \mu_h}{2\mu_e} \quad (4.1)$$

Here we further assume the effective movement of electrons and holes are purely due to applied electrical field. So for bulk Si where  $\mu_e \gg \mu_h$ , we will have  $\alpha_e \approx \alpha$ . If  $\mu_e \approx \mu_h$ ,  $\alpha$  will be reduced to half of its theoretical value, which has already been observed experimentally [111]. Using the fitted value of  $\alpha$  in Table 4.1, we estimate that  $\mu_e \approx 1.4\mu_h$ . The balanced electron and hole mobility values suggest that electrons and holes have a high probability to form excitons right in the 1:5 SiNC emission layer, resulting in a high or nearly-unity charge balance factor  $\gamma$ .

Hole conductivity experiments are conducted using Au as contacts (Figure 1.6(b)), but turn out unsuccessful. The main reason is that Au, which is deposited at high temperature, may diffuse in the SiNC layer and induce unintentional doping or even short the device, especially for thinner NC films. Therefore we switch to time-of-flight (TOF) method to further explore the electrical properties in SiNCs.

### 4.3 Carrier Mobility in Silicon Nanocrystals

Few literatures [30, 112-114] have been reported before to evaluate the mobility of NCs using TOF technique. One reason is that it is often difficult to prepare a “thick” thin NC thin film and the as-prepared films have much larger RC delay time than typical organics, which could induce significant inaccuracy in the TOF measurement.

To check feasibility of TOF on our SiNCs, we first calculate the absorption length ( $\lambda$ ) of SiNCs as  $\sim 10$  nm, using an absorption coefficient of  $\sim 10^6$  cm<sup>-1</sup> at 337 nm pump wavelength [73]. Therefore, in a 300 nm thick thin film, it is reasonable to suppose that all the charge carriers are generated at or very close to the illuminated side (in our case,

ITO and SiNC interface). Further assuming that the carriers could drift to the opposite side under electrical field without any trapping, hopping or dispersion due to material inhomogeneity, mobility can thus be determined using Equation (4.2):

$$\mu = \frac{v}{F} = \frac{d/t_r}{V/d} = \frac{d^2}{vt_r} \quad (4.2)$$

In which  $v$  is the velocity of charge carriers and  $t_r$  is the time of travel. The device thickness  $d$  can be measured with scanning probe microscopy as discussed earlier and transit time  $t_r$  can be read when the photocurrent (or photovoltage) vanishes. In more realistic cases, due to a spatial distribution of generated charge carriers,  $t_r$  is often taken as the midpoint of the decreasing transient photocurrent curve.

As in the case of NCs [30], charge transport in SiNCs is expected to be dispersive, where there is a significant distribution of inter-particle hopping times. Scher and Montroll [115] developed a detailed theoretical treatment to deal with such dispersive transients. They proposed that a considerable proportion of generated charge carriers will start to drift immediately after formation; while others will be immobilized to some long-range hopping sites (traps, for example) and will exhibit a longer transit time. As such, the transient photocurrent will be composed of one fast decay term and another slow decay term, which can be written as:

$$V(t) \propto \begin{cases} t^{-(1-\delta)}, & t \ll t_r \\ t^{-(1+\delta)}, & t \gg t_r \end{cases} \quad (4.3)$$

In (4.3),  $\delta$  is a factor that characterizes the degree of dispersion or amorphism in the material, with 0 for purely crystalline and 1 for completely amorphous. In our SiNCs,  $\delta$  typically has a value of  $0.3 \pm 0.05$ , regardless of surface ligand coverage.

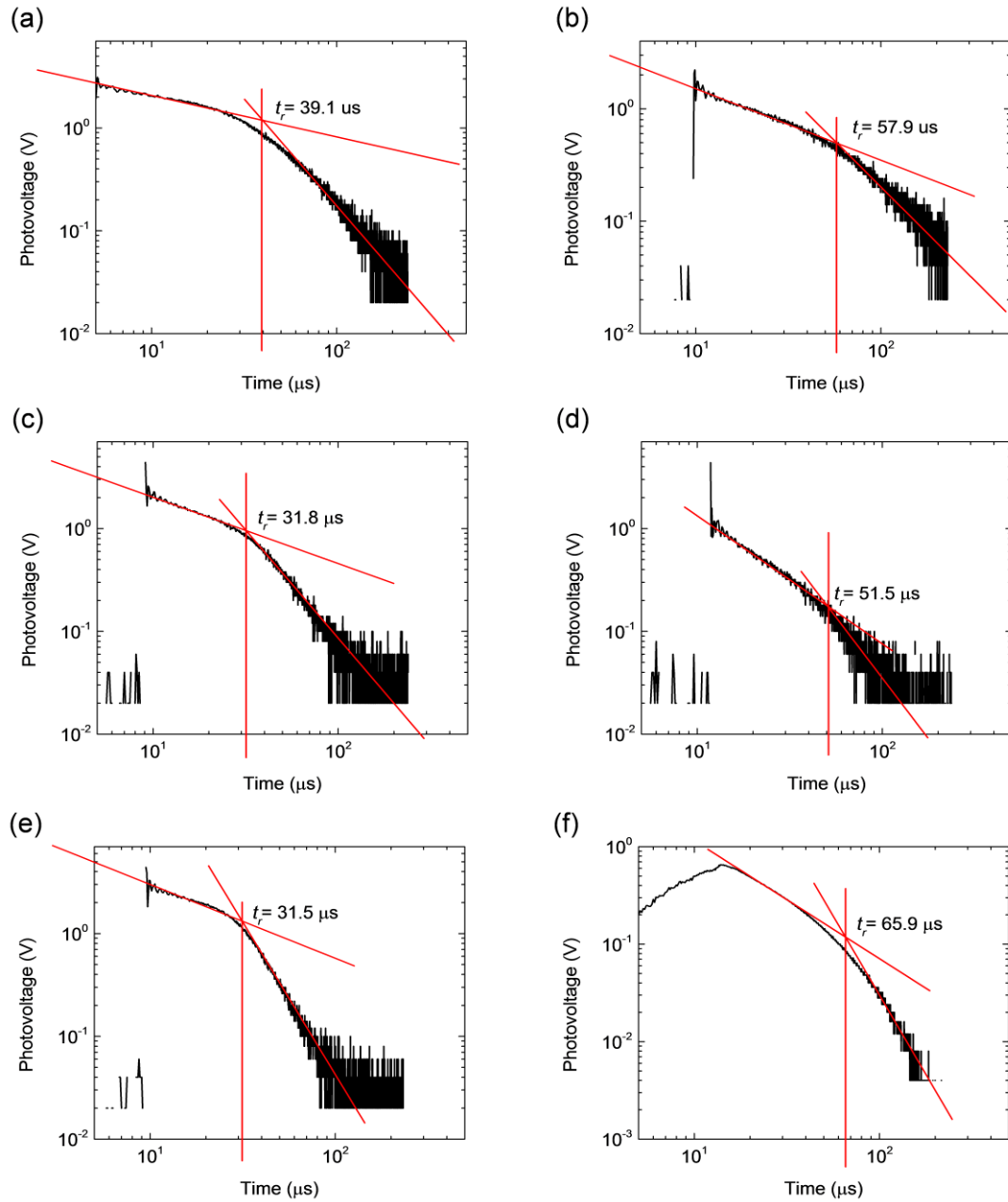


**Figure 4.2** Time-of-flight mobility measurements of SiNCs: electron mobility in **(a)** 1:5 sample, **(c)** 1:1000 sample and **(e)** 1:2000 sample; and hole mobility in **(b)** 1:5 sample, **(d)** 1:1000 sample and **(f)** 1:2000 sample.

The transient photocurrent decay curve plotted in log-log scale can therefore be fitted with two straight lines and the intersection of these two lines is found to be the

transit time  $t_r$ . The physical meaning of  $t_r$  in fact is the time that “faster” charge carriers travel in the device.

The decay curves for 1:5, 1:1000 and 1:2000 SiNC samples are shown in Figure 4.2, and the extracted parameters are summarized in Table 4.2. All the data are obtained at 30 V.

SiNCs ( $d=300$ nm)	1:5	1:1000	1:2000
$t_r$ for electrons ( $\mu\text{s}$ )	39.1	31.8	31.5
$t_r$ for holes ( $\mu\text{s}$ )	57.9	51.1	65.9
$\mu_e$ ( $\text{cm}^2\text{V}^{-1}\text{s}^{-1}$ )	$7.87 \times 10^{-7}$	$9.43 \times 10^{-7}$	$9.52 \times 10^{-7}$
$\mu_h$ ( $\text{cm}^2\text{V}^{-1}\text{s}^{-1}$ )	$5.32 \times 10^{-7}$	$5.86 \times 10^{-7}$	$4.56 \times 10^{-7}$
$\mu_e/\mu_h$	1.48	1.61	2.09

Table 4.2 Summary of 1:5, 1:1000 and 1:2000 SiNC electron and hole mobilities.

Interestingly, for 1:5 SiNC sample, it is found that  $\mu_e \approx 1.48\mu_h$ , very close to the derivation in section 4.2.1. This supports the use of an Ohmic conduction model with a Poole-Frenkel mobility to fit the  $J$ - $V$  curve in Sec. 4.2. Also interesting is that, the mobility values for both electrons and holes in 1:1000 and 1:2000 samples are typically higher. This is not surprising since 1:1000 and 1:2000 samples are covered with fewer surface ligands.

It is also interesting to compare these mobility values with our previous study [34], in which different electron transport materials with different thicknesses are utilized to fabricate SiNC-OLEDs. It is found that the device EQE changes only a little when using high electron mobility chemicals, such as N,N'-dicarbazolyl-4,4'-biphenyl (CBP,  $\mu_e \sim 5 \times 10^{-4} \text{ cm}^2\text{V}^{-1}\text{s}^{-1}$  at 0.5 MV/cm [116]). However, EQE suffers significantly when 40 nm low electron mobility material 4,4',4''-tris-(N-carbazolyl)-triphenylamine (TCTA,

$\mu_e \sim 10^{-8} \text{ cm}^2 \text{ V}^{-1} \text{ s}^{-1}$  [117]) is used. This suggests that charge transport in our SiNC-OLEDs is limited by the low mobility (on the order of  $10^{-7} \text{ cm}^2 \text{ V}^{-1} \text{ s}^{-1}$ ) of SiNCs. A wide range of higher mobility organic semiconductors become possible candidates for fabricating SiNC-OLEDs as long as their energy levels could confine excitons in the SiNC emission layer (Figure 2.3).

If we take the electron mobility value and conductivity extracted from  $J$ - $V$  measurements using Equation (1.12), the carrier density is  $5 \times 10^{16} \text{ cm}^{-3}$ , 6 orders of magnitude higher than intrinsic carrier density  $n_i$  in bulk Si. To explain this huge difference, the field dependent mobility also needs to be taken into consideration. If we further apply the Poole-Frenkel coefficient  $\alpha$  from Table 4.1, the corrected carrier density is  $6 \times 10^{13} \text{ cm}^{-3}$ , which is smaller than the value ( $4 \sim 9 \times 10^{14} \text{ cm}^{-3}$ ) reported in [107], in which SiNCs are capped with  $\text{SiO}_2$  shell. The difference is likely due to change in surface conditions.

Mobility measurement at different electrical field is unsuccessful. At lower field, the plot only reveals a single linear decay (instead of two) in log-log scale, which might result from the fact that not all the generated excitons are effectively dissociated. While at higher field, the device easily breaks down.

As pointed at the beginning of this section, to strictly evaluate the transit time  $t_t$ , the RC delay of the time-of-flight testing circuit is also calculated. Taking the device as a planar capacitor, the capacitance can be determined using Equation 4.4. Here we take bulk Si dielectric constant ( $\epsilon_r=11.7$ ) and use device area  $A=9 \times 10^{-6} \text{ m}^2$  and thickness  $d=300 \text{ nm}$ ,  $C$  is calculated as about 3 nF.

$$C = \frac{\epsilon_r \epsilon_0 A}{d} \quad (4.4)$$

The resistance used the experiment is 1000  $\Omega$ . Thus the RC delay time constant is about 3  $\mu\text{s}$ , which is an order of magnitude smaller than  $t_r$ . To further decrease the RC delay time and make more accurate measurements on mobility, a 50  $\Omega$  resistor is also tried. However in this situation, the initial faster decay is too small to be detected.

#### 4.4 Summary

In this Chapter, electrical properties of SiNCs with different degrees of surface ligands passivation are measured with current-voltage ( $J$ - $V$ ) and time-of-flight (TOF) measurements. It has been found that 1:5 SiNCs are characterized by Ohmic conduction with zero-field electron conductivity on the order of  $10^{-8} \Omega^{-1}\text{cm}$ , and Poole-Frenkel coefficient  $\sim 5 \times 10^{-3} \text{ cm}^{0.5}\text{V}^{-0.5}$ . Both electron and hole mobilities are obtained with TOF technique, with their values are on the order of  $10^{-7} \text{ cm}^2\text{V}^{-1}\text{s}^{-1}$ . With less surface ligand coverage, the difference between electron and hole mobility increases, which could help explain the decrease in  $\gamma$  and EQE in our SiNC-OLEDs.

## Chapter 5 Silicon Nanocrystal Photoluminescence

### 5.1 Foreword

In the previous chapter, the electron and hole mobilities of SiNCs passivated with differing degrees of surface ligands coverage were characterized. The mobility imbalance could be a possible reason for the decrease in efficiency at high current density observed SiNCs. However, it is also possible that ligand coverage could also induce changes in the PL efficiency ( $\eta_{PL}$ ).

In the research of PL from SiNCs, two questions remains in debate. One is the origin of PL in SiNCs. Some of the literature argues that the PL in SiNCs originates from core states, due to strong quantum confinement. Their proof mainly comes from characteristic-phonon-assisted PL [81], size dependent emission energy [68, 118], and sensitivity of PL spectra to large pressure [119]. While other reports argue that the emission is related to the surface defects in the SiNCs. Experimental support arises from sensitivity to chemical treatments [120], insensitivity to large magnetic fields [121], and long-lived PL decay (on the order of  $\mu\text{s}$ ) [122]. There is also work arguing that both surface and core states contribute to PL [17].

Another interesting topic is the decay mechanism and formula for transient PL. Most researchers [10, 123-128] are inclined to use stretched exponential (Equation (1.29)). To explain the deviation from ideal single exponential decay, Auger process [124] and exciton transfer process [128] are often considered. However, no solid experimental proof has been offered. Other mechanisms are also proposed. For example, a two-level system [129] has been considered due to possible a singlet-triplet transition at low

temperature; multi-exponential decay fit [83] has been used due to size distribution in SiNCs; bi-exponential is utilized to explain two different types of emission states (surface and core) [17]; and single exponential is used by people who believe core-only or surface-only emission [68, 130].

In this chapter, we will explore these questions and offer insight into the underlying mechanisms of PL in SiNCs through series of surface ligand coverage dependent, temperature dependent and size dependent PL experiments.

## **5.2 Room Temperature Photoluminescence**

To examine whether ligand coverage plays an important role in SiNC PL, the thin film PL was measured at room temperature, as described in Chapter 3. Due to rapid oxidation (especially under UV light exposure) in samples with fewer ligands, PL is measured immediately after removing the samples from a N<sub>2</sub> glovebox. The steady-state and transient PL behaviour are plotted in Figure 5.1 (a) and (b) respectively.

Interestingly, it is found that changes in surface ligand coverage do not play a significant role in impacting emission wavelength, intensity and exciton lifetime, as listed in Table 5.1. In other words, surface modification does not significantly change the PL in SiNCs, which suggests that the origin of PL is core emission.

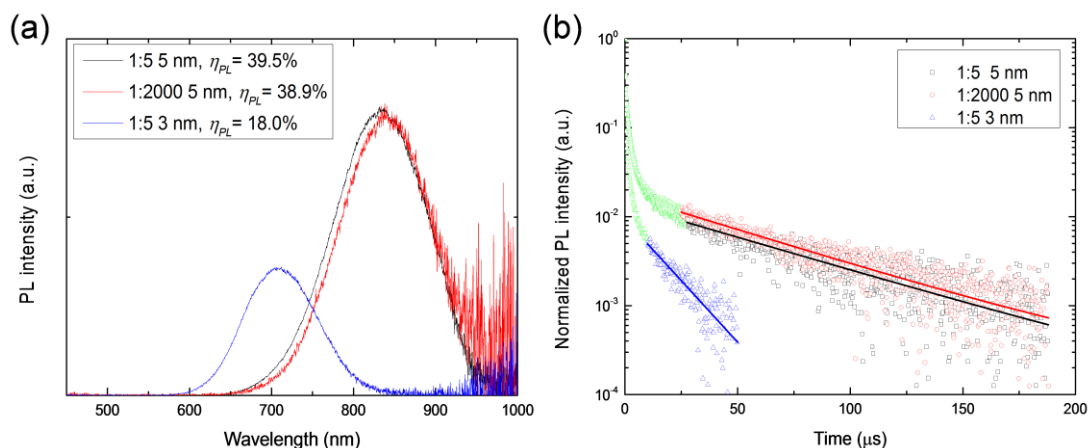


**Figure 5.1** (a) Steady-state photoluminescence spectra and (b) transient photoluminescence decay of 1:5 5 nm ( $\square$ ), 1:2000 5 nm ( $\circ$ ) and 1:5 3 nm ( $\triangle$ ) SiNCs thin film. The masked data points are in green and the rest points are fitted with a single exponential decay (straight line in the plot).

Size (nm)	5	5	3
Ligand ratio	1:5	1:2000	1:5
Peak wavelength (nm)	834	839	711
$\eta_{PL}$	39.5%	38.9%	18.0%
$\tau$ ( $\mu\text{s}$ )	59.7	58.8	16.6
$k_r$ ( $\times 10^3 \text{ s}^{-1}$ )	6.62	6.62	10.84
$k_{nr}$ ( $\times 10^3 \text{ s}^{-1}$ )	10.1	10.4	49.4

**Table 5.1** Summary of steady-state and transient photoluminescence measurements on SiNCs with varying size and ligand coverage ratio at room temperature (296 K).

For the transient PL decay, the stretched exponential fails to provide a good fit. Here we select the region where the curvature ends (typically under  $\sim 1\%$  of normalized peak intensity in this testing configuration) and fit with a single exponential. A similar method has been used before in both CdSe NCs [60] and SiNCs [68]. The authors of these papers attribute the faster decay at short times to either the laser pulse or RC delay of the detection circuit. In our measurement, the lifetime of faster decay is  $\sim 1 \mu\text{s}$ , which is much

slower than the pulse width of the laser (800 ps). We also tried to measure steady-state spectrum using pulsed laser (Figure 5.2). Due to extremely small duty cycle ( $\sim 10^{-8}$ ), the signal to noise ratio is low. However, no emission peak other than SiNCs is observed, proving that neither laser nor colored glass filter emission play a role in the transient PL decay.

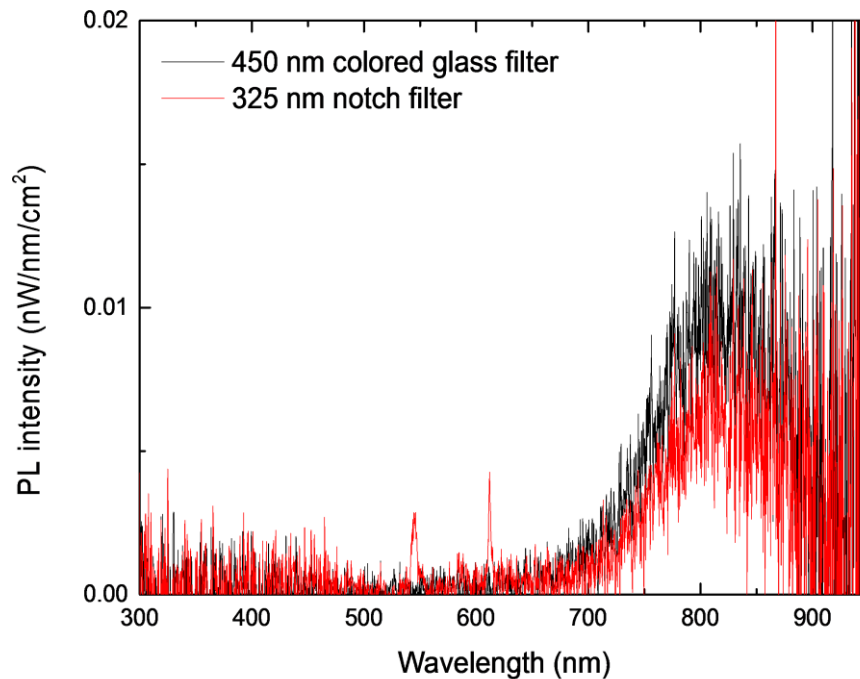


**Figure 5.2** Photoluminescence emission spectra of SiNCs excited by a pulsed laser (duty cycle  $\sim 10^{-8}$ ). The colored glass is a low-pass filter which cuts off the emission over 450 nm in wavelength. The notch filter is OD 4 and has a reflectivity >99.99% around its central peak wavelength (325 nm).

For the 1:5 5 nm SiNCs thin film sample, transient PL is collected as a function of illumination intensity, as shown in Figure 5.3. The extracted lifetimes are similar: at 34  $\text{mJ}/\text{cm}^2$ ,  $\tau=59.7 \mu\text{s}$ ; at 16  $\text{mJ}/\text{cm}^2$ ,  $\tau=58.8 \mu\text{s}$ ; and at 5.5  $\text{mJ}/\text{cm}^2$ ,  $\tau=60.4 \mu\text{s}$ . For the sample with highest intensity, the calculated number of photons in the illuminated region (6.6  $\text{mm} \times 3 \text{ mm} \times 160 \text{ nm}$ ) is  $\sim 1.2 \times 10^{15}$ , which is 3 orders of magnitude higher than the

number of SiNCs ( $\sim 6.7 \times 10^{12}$ ). No additional exciton decay routes open even with such high exciton concentration. This suggests that Auger process is unlikely to occur in our SiNCs over these ranges.

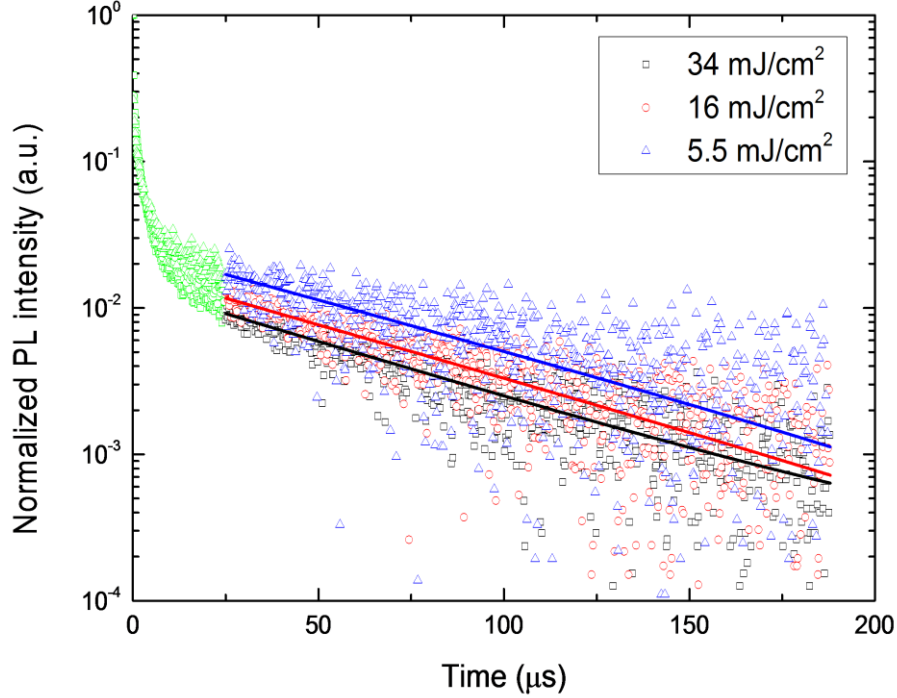


**Figure 5.3** Transient photoluminescence decay of 1:5 5 nm SiNCs at different pump intensities,  $\square$ : 34 mJ/cm<sup>2</sup>,  $\circ$ : 16mJ/cm<sup>2</sup> and  $\triangle$ : 5.5 mJ/cm<sup>2</sup>. The masked data points are in green, and are not included in the fit (straight lines in the plot).

Using the values of  $\eta_{PL}$  and  $\tau$ , we also could calculate both radiative ( $k_r$ ) and non-radiative ( $k_{nr}$ ) decay rates using Equation (1.25). For smaller SiNCs,  $k_r$  is higher, which can be explained by the increase in spatially overlapped wavefunction [2]. However, it still remains unclear why  $k_{nr}$  varies with NC size. To study the origin of this observation, we conduct temperature dependent measurements. As 1:5 and 1:2000 samples show almost identical optical properties, only 1:5 (5 nm and 3 nm) samples are tested later.

## 5.3 Temperature Dependent Photoluminescence

### 5.3.1 Steady-state Photoluminescence

Figure 5.4 shows steady-state PL collected as a function of temperature. It is found that as the temperature decreases, integrated PL intensity and energy bandgap both increase. Here, we simply take  $\frac{hc}{\lambda_{peak}}$  as the bandgap energy, similar as in [127].

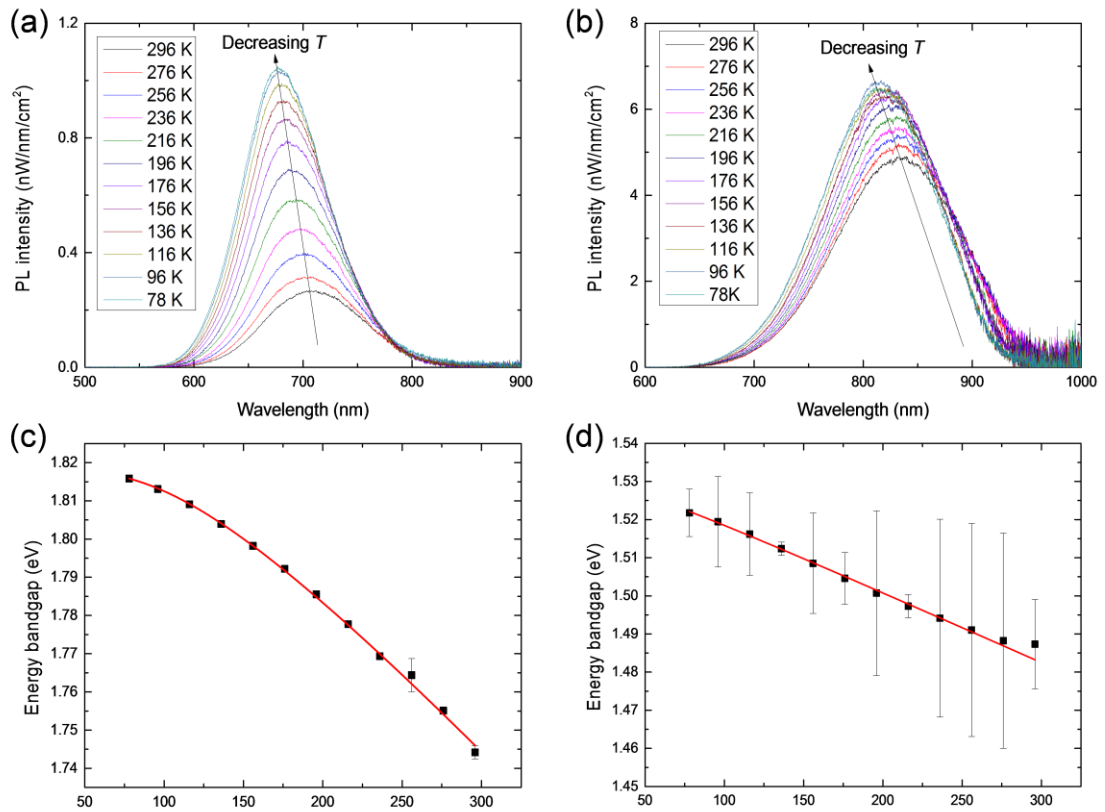


**Figure 5.4** Steady-state photoluminescence spectra for (a) 3 nm and (b) 5 nm SiNCs at different temperatures, and energy bandgap of (c) 3 nm and (d) 5 nm SiNCs at different temperatures.

The temperature dependence of the energy bandgap in bulk semiconductors is usually explained by Varshni's formula [131], which states that:

$$E_g(T) = E_g(0) + \frac{AT^2}{T+B} \quad (5.1)$$

In this equation,  $E_g(0)$  is the bandgap at 0 K,  $A$  and  $B$  are material constants. In [131], Varshni relates  $B$  to Debye's temperature. However, this assumption carries no physical background and fails to explain bulk Si (fitted value 1108 K, compared with theoretical value 645 K). Significant offset in fitting with this equation is also observed in SiNCs [127].

It is known that thermal contraction induced size change on NCs could induce additional confinement [2]. However, using the thermal expansion coefficient of bulk Si [132], the calculated reduction in NC size is small ( $<10^{-4}$ ), so this possibility is ruled out.

In order to explain the temperature dependence, we follow the model in [133], in which the bandgap  $E_g$  is described as:

$$E_g(T) = E_g(0) - S \frac{\langle \hbar\omega \rangle}{\exp\left(\frac{\langle \hbar\omega \rangle}{k_B T}\right) - 1} \quad (5.2)$$

where  $S$  is the electron-phonon coupling coefficient,  $\langle \hbar\omega \rangle$  is the average phonon energy, and the expression,  $\frac{1}{\exp\left(\frac{\langle \hbar\omega \rangle}{k_B T}\right) - 1}$  is Planck's distribution function of phonons. This model assumes that electrons in the valence band could cross the bandgap with the aid of ambient phonons. As the temperature decreases, there are fewer phonons at the average energy to participate in this process, making the transition more difficult. The fitted values are listed in Table 5.2.

NC size	$E_g(0)$	$\langle \hbar\omega \rangle$	$S$
3 nm	1.82 eV	29.7 meV	5.31
5 nm	1.53 eV	9.0 meV	2.15

**Table 5.2** Zero temperature bandgap, average phonon energy and coupling coefficient of 3 nm (Figure 5.4 (c)) and 5 nm SiNCs (Figure 5.4 (d)) using Equation (5.2).

In 3 nm SiNCs, the average phonon energy  $\langle \hbar\omega \rangle$  is 29.7 meV, which is close to the reported value of bulk Si (25.5 meV) [133]. The small difference could be due to additional momentum conservation phonons in NC system. However, the fitted value for 5 nm sample is only 9 meV, which deviates greatly from bulk value. One possible reason is that the energy bandgap in close packed NC solid is not dominated by individual NCs, but a collective behavior [19]. In larger SiNCs (5 nm) where the inter-particle separation is longer, potential overlap of wavefunctions between adjacent NCs is reduced. In smaller NCs (3 nm), on the other hand, exciton wavefunctions overlap much more, and could be continuous even including interparticle barriers, which is comparable to bulk materials where wavefunction is continuous everywhere.

It is also interesting to study the change in PL intensity and shape as a function of temperature. The spectrum appears as a single Gaussian peak between 78 K to 296 K, which supports our idea that the only one emission state exists in the SiNCs. Further, as surface modification changes only a little in  $\eta_{PL}$ , it is concluded that this emission must be from core states.

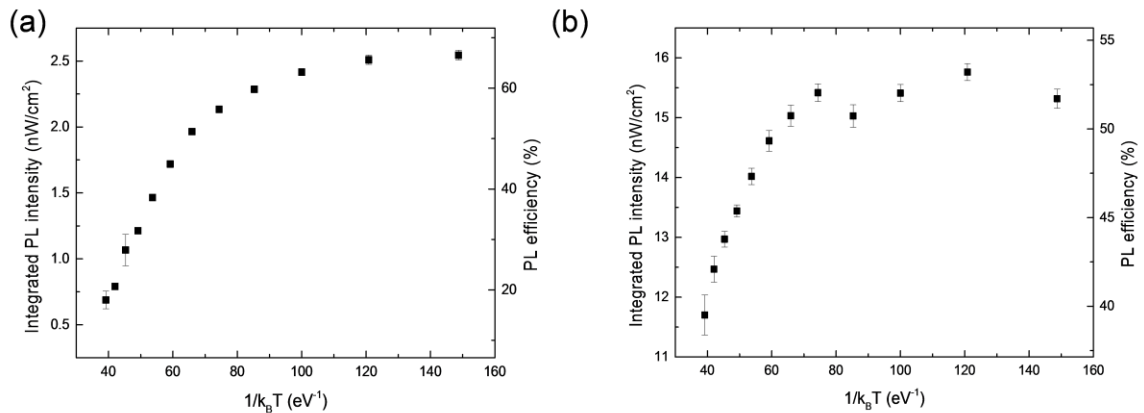


**Figure 5.5** PL efficiency ( $\eta_{PL}$ ) derived from integrated PL intensity versus temperature of (a) 3 nm and (b) 5 nm SiNCs.

In Figure 5.5, we plot  $\eta_{PL}$  versus temperature by integrating the area under the spectra, assuming that absorption does not strongly change over the studied temperature range. In order to further extract the values of  $k_r$  and  $k_{nr}$ , temperature dependent lifetime study is also conducted.

### 5.3.2 Transient Photoluminescence

The PL transient decay of 1:5 5 nm and 3 nm SiNCs at different temperatures are shown in Figure 5.6. At room ambient measurement, the top region ( $\sim 90\%$  intensity) is not included in the fitting. As the testing is performed in an optical cryostat which limits the collection of PL emission, signal to noise ratio is typically lower. It is also noticed that the proportion of top region changes from  $\sim 99\%$  to  $\sim 90\%$ , but the fitted lifetime at room temperatures are similar (see Figure 5.7). This invalidates the assumption that two different types of emission states are involved in SiNC PL, as the real transient decay rate does not depend on collection geometry.

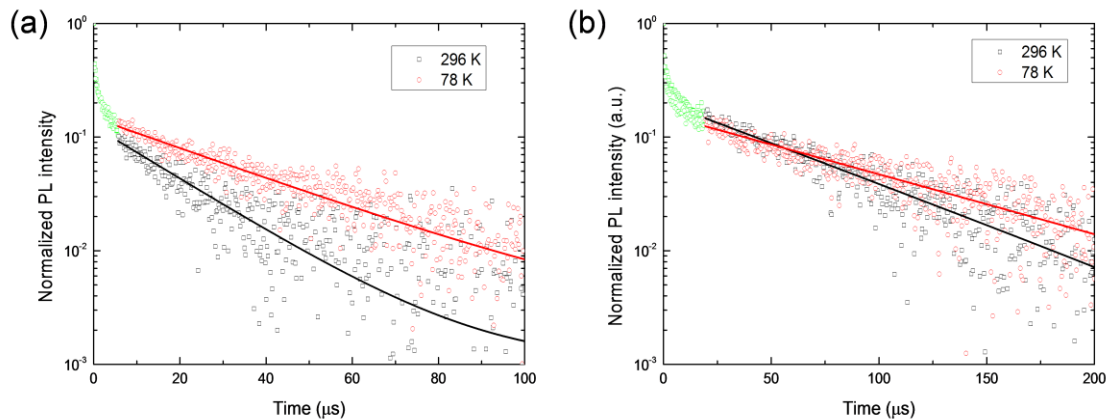


**Figure 5.6** Transient photoluminescence decay curve at 296 K ( $\square$ ) and 78 K ( $\circ$ ), **(a)** 1:5 3 nm SiNCs and **(b)** 1:5 5 nm SiNCs. The masked data points are in green.

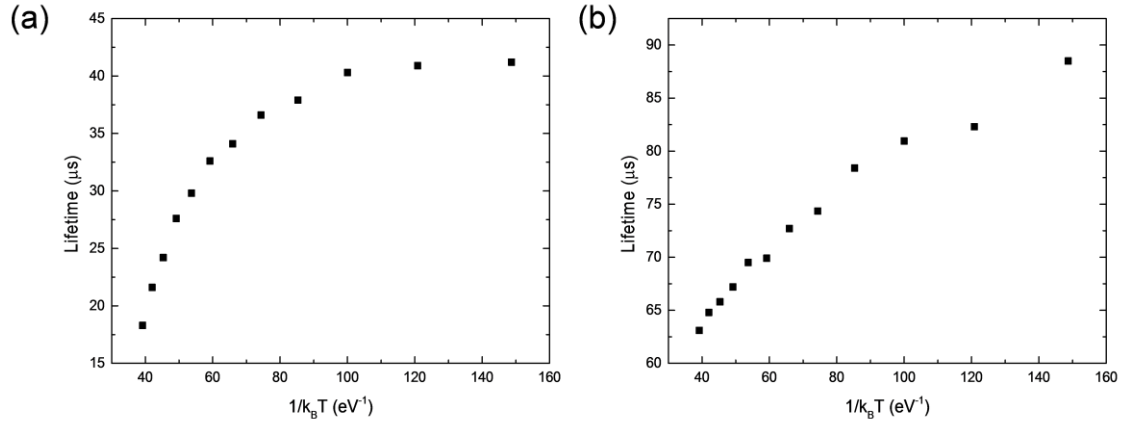


**Figure 5.7** Fitted lifetime values of **(a)** 3 nm SiNCs and **(b)** 5 nm SiNCs at different temperatures.

Using Equation (1.25), Figure 5.5 and 5.7, radiative and non-radiative exciton decay rates ( $k_r$  and  $k_{nr}$ ) at different temperatures are calculated, as shown in Figure 5.8.  $k_r$  in 3 nm SiNCs is higher than in 5 nm, which is likely due to the increase in wavefunction overlap [2]. However, different from the assumption in some literatures [61, 63, 127],  $k_r$  is found not to be a constant with temperature. In CdSe NCs [60], it is argued that two types of radiative decay exists: direct recombination and phonon-assisted recombination, which is temperature dependent. This argument might be helpful to explain the change of  $k_r$  with temperature in SiNCs.

For the non-radiative decay rate ( $k_{nr}$ ), we find it to be thermally activated, which follows Arrhenius's law with an additional constant term  $k_0$  taken into account:

$$k_{nr}(T) = k_a \exp\left(-\frac{E_a}{k_B T}\right) + k_0 \quad (5.3)$$

Fitting results are listed in Table 5.3. It is found that at low temperature where the non-radiative process is effectively quenched,  $\eta_{PL}$  still deviates greatly from unity. This can be explained by the constant term  $k_0$  in Equation (5.3), which is probably from the indirect

bandgap nature in Si. Similar argument [68] has been made previously which states that SiNCs are still indirect or quasi-direct bandgap materials even with momentum breakdown due to uncertainty principle.

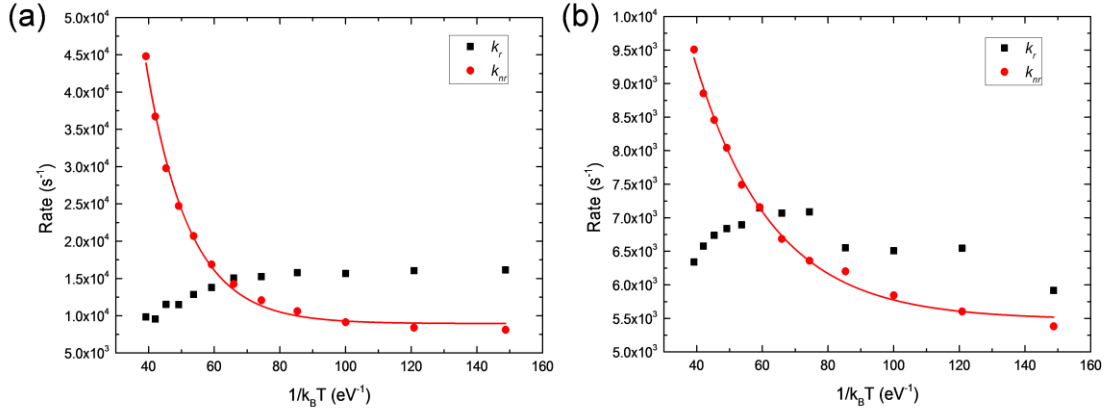


**Figure 5.8** Calculated radiative ( $k_r$ ) and non-radiative exciton decay rate ( $k_{nr}$ ) at different temperatures of (a) 3 nm SiNCs and (b) 5 nm SiNCs.

NC size	$k_a$	$E_a$	$k_0$
3 nm	$6.94 \times 10^5 \text{ s}^{-1}$	76.3 meV	$8.95 \times 10^3 \text{ s}^{-1}$
5 nm	$2.07 \times 10^4 \text{ s}^{-1}$	42.6 meV	$5.48 \times 10^3 \text{ s}^{-1}$

**Table 5.3** Decay rates and activation energy of 3 nm (Figure 5.8 (a)) and 5 nm SiNCs (Figure 5.8 (b)) using Equation (5.3).

$E_a$  is the activation energy of non-radiative decay and is greater in smaller SiNCs, which could be related to the exciton binding energy in SiNCs [4]. As the size of NC decreases, dielectric constant will go down, which will increase the exciton binding energy according to Bohr's model [64]. We notice that our experimental value is smaller than the calculated value (82 meV for 3 nm SiNCs) in literature [134]. This is probably because in the calculation, dielectric constant is taken as a constant with temperature, while in our case, temperature may play a significant role.

## 5.4 Summary

In this Chapter, PL of SiNCs thin film samples with different degrees of surface ligand passivation and with different sizes are characterized by steady-state and transient measurements at different temperatures. It has been found that surface modification does not strongly affect  $\eta_{PL}$  in SiNCs. Further, through the single exponential fitting of transient PL, it is concluded that the origin of PL in SiNCs is only due to core emission states. We also noticed that electron-phonon coupling is likely responsible for the energy bandgap broadening in SiNCs as temperature decreases. In addition,  $k_{nr}$  of SiNCs is explained with an Arrhenius equation, in which the activation energy is probably the exciton binding energy and the constant term is due to the indirect bandgap nature in SiNCs.

## Chapter 6 Conclusion and Future Research Proposal

### 6.1 Conclusion

The main goal of this thesis is to investigate device physics and study the origin of high efficiency in Si NC-OLEDs. This was done by thoroughly characterizing the electrical and optical properties in SiNCs. A deeper understanding of these properties in SiNCs might be beneficial for designing highly efficient Si NC-OLEDs and other NC-OLEDs as well. This chapter will sum up the results achieved so far and propose future directions for research.

In Chapter 4, the electrical conductivity and mobility in SiNCs with different degrees of surface ligand coverage were measured. It was found that electron transport in SiNCs is defined by Ohmic conduction with an electrical field-dependent mobility. Electron and hole mobilities, determined with the help of time-of-flight (TOF) measurements, are both on the order of  $10^{-7} \text{ cm}^2\text{V}^{-1}\text{s}^{-1}$ . This suggests that the transport in Si NC-OLEDs is limited by the SiNC layer and further supports the exciton confinement model proposed previously. In addition, as the degree of ligand coverage decrease, an increased mobility imbalance is observed which might explain the drop in external quantum efficiency.

In Chapter 5, a complete photoluminescence (PL) study was performed. Ligand coverage dependent studies at room temperature reveal that surface modification does not strongly impact the PL in SiNCs. Pump power dependent studies shows that Auger exciton recombination process is unlikely. Size dependent studies show that smaller SiNCs tend to have a larger exciton decay rate.

More interestingly, temperature dependent PL experiment supports the thought that the emission in SiNCs is due only to core states. Both the energy bandgap and PL intensity of SiNCs increase as the temperature is reduced. The former is explained through electron-phonon coupling model. The latter is due to the reduction of non-radiative decay rate ( $k_{nr}$ ), which is characterized by Arrhenius law. The activation energy ( $E_a$ ) of  $k_{nr}$  is likely from exciton dissociation.

## 6.2 Charge Mobility using Lateral Patterned Devices

In Chapter 4, the vertical device structure (Figure 4.1(b)) was tried to extract mobilities from current-voltage measurement. However, limited by the spin-coating technique, device thickness is typically smaller than 300 nm so that device tends to break down due to high current density before entering SCLC regime. For the same reason, hole measurement is unsuccessful due to the high diffusivity of Au atoms (top metal contact) at high temperature. More importantly, uniformity in thickness is always a problem. Thickness difference exists between center and corner, especially at low spinning rate.

In order to solve these problems, an interdigitated lateral device architecture will be used, as show in Figure 6.1. The device has 100 sets of electrodes (channels) in total and the spacing (channel width  $L$ ) between each two adjacent electrodes is fixed at 5  $\mu\text{m}$ , which on average could give a more accurate result than a single vertical device. The SiNCs are spun-coated into the channel without further high temperature treatment. The metal electrodes will be either Al or Au, which allows electron-only or hole-only

transport, as discussed earlier. The electrodes are deposited before spin-coating process so that metal diffusion will not become a problem.

To further clarify the transport mechanism, the interdigitated lateral device will first be tested in standard two probe  $J$ - $V$  measurement. Due to a larger device thickness, a high voltage source (up to 200 V) will be used for the testing.

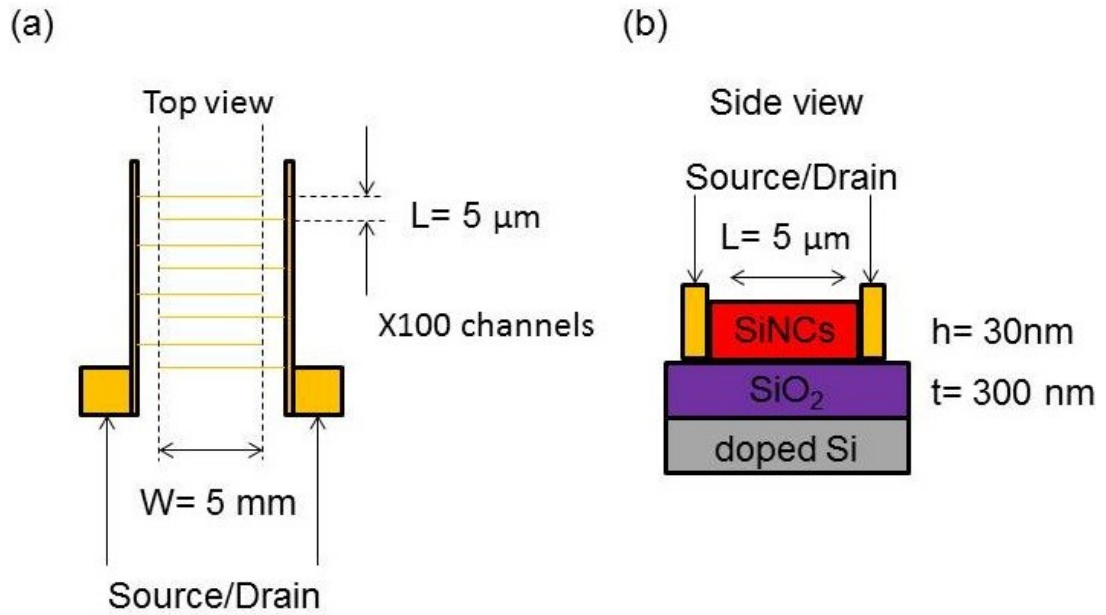


**Figure 6.1** Top view (a) and (b) side view of the interdigitated lateral device.

The advantage of this device is it can also be tested as a FET. At low drain voltage ( $V_d$ ), drain current ( $I_d$ ) increases linearly with  $V_d$ , the mobility in this regime ( $\mu_{lin}$ ) can be calculated from the slope of  $I_d$  vs.  $V_g$  plot, as shown in Equation (6.1).  $V_g$  is the gate voltage,  $L$  is channel length,  $W$  is channel width and  $C'$  is the capacitance of silica layer per unit area, which can be calculated using Equation (6.2). At high  $V_d$  ( $V_d \gg V_g - V_T$ , where  $V_T$  is the threshold voltage), mobility tend to saturate and can be calculated using Equation (6.3).

$$\mu_{lin} = \frac{\partial I_d}{\partial V_g} \frac{L}{cV_d W} \quad (6.1)$$

$$C' = \frac{\epsilon_{SiO_2}}{t} \quad (6.2)$$

$$\mu_{sat} = \left( \frac{\partial \sqrt{I_d}}{\partial V_g} \right)^2 \frac{2L}{C'W} \quad (6.3)$$

The mobility at zero electrical field in Ohmic conduction regime  $\mu_0$  can be approximately taken as  $\mu_{lin}$ , so from Equation (1.12), carrier density  $n$  can also be extracted. The obtained values of  $n$  and  $\mu_{sat}$  could also be compared with the results from TOF measurements. This experiment could serve as an additional proof for the mobility of SiNCs.

## 6.3 Spin Fraction in Hybrid SiNC-OLEDs

### 6.3.1 Exciton Spin Fraction Measurement

As discussed earlier, typically allowed emitting fraction for exciton states in organic emitter is 25% for the fluorescent OLEDs and 100% for phosphorescent OLEDs. The increase of spin fraction in phosphorescent materials is mainly due to strong spin-orbit interaction, where triplet states (75% of the total excitons) could be allowed for radiative recombination [91]. In phosphorescent OLEDs, usually an organometallic chemical that contains a heavy metal atom, such as Iridium (Ir), is involved. The heavy element, which has a high orbital momentum, could help overcome the momentum conservation and facilitate triplet recombination. While exciton spin fraction has been well studied in organic semiconductors [91, 135-137], to our best knowledge, very few researches have been conducted to define and confirm spin statistics of the exciton states in highly

luminescent SiNCs.

Silicon, as a light atom, is usually considered not able to support enough orbital momentum, nor giving phosphorescence. But it should be mentioned that it is still possible for over 25% of the total exciton states to contribute to the SiNC EL. In fluorescent OLEDs, the increase in spin fraction could happen via several possible mechanisms, for example: thermally activated delayed fluorescence (TADF) [138, 139], triplet-triplet annihilation [140] and exciton transfer process [43, 141]. Details on these mechanisms will be discussed later, and right now we will focus on accurately determining the value of exciton spin fraction  $\chi$ .

If we rearrange Equation (2.1), spin fraction  $\chi$  can be written as follows:

$$\chi\gamma = \frac{\eta_{EQE}}{\eta_{PL}\eta_{OC}} \quad (6.4)$$

Following the discussions earlier, the device  $\eta_{EQE}$  has a peak value of 8.6% [34]. And if we further take  $\eta_{PL}$  as 40%,  $\eta_{OC}$  as ~20% and  $\gamma$  as unity due to mobility balance in our 1:5 SiNC-OLEDs, the calculated  $\chi$  is close to 1, suggesting that almost every exciton generated in SiNC-OLEDs could contribute to the radiative recombination. This estimation is surprising. Thus, experiments that can accurately measure the spin fraction definitely need to be conducted.

Segal et al. developed a method to measure the upper limit of the excitonic statistics in fluorescent OLEDs [137], which could also be utilized to probe the spin fraction in SiNC-OLEDs. The experimental setup is shown in Figure 6.2. A 405 nm CW laser is employed to excite the device. The laser beam is right aligned with device cathode. The excited PL is collected by a silicon photodiode after passing through a 450 nm colored

glass filter. Under reverse bias, the PL intensity will be quenched by a certain amount because the applied electrical field could dissociate some generated excitons into charges. Assuming  $k_e$ , the quenching rate of excitons due to electrical field, is small and independent of field,  $\Delta P_{PL}$ , the differential PL power, is given by:

$$\Delta P_{PL} = P_{PL}(k_e) - P_{PL}(k_e = 0) = -\eta_{OC} h\nu \frac{k_e}{k_r + k_{nr}} \phi \quad (6.5)$$

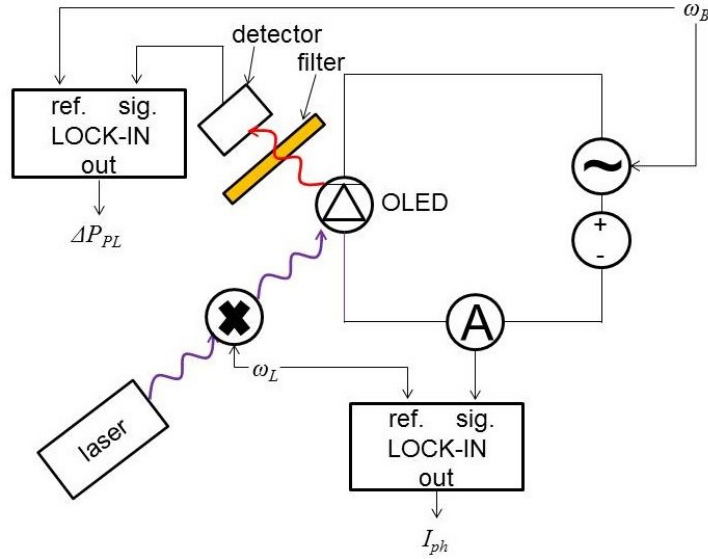


**Figure 6.2** Testing geometry of two-tone synchronous spin fraction measurement.

In this equation,  $\nu$  is the frequency of emitted photons in SiNC layer, and  $\Phi$  is the photon flux. Meanwhile, the charges that are formed from the dissociated excitons could also be measured. The generated photocurrent,  $I_{ph}$ , can thus be written as equation 6.6.

$$I_{ph} = e \frac{k_e}{k_r + k_{nr}} \phi \quad (6.6)$$

Combing Equation (6.4) to (6.6), we can obtain:

$$\eta_{OC} \eta_{PL} = -\frac{e}{h\nu} \frac{\Delta P_{PL}}{I_{ph}} \quad (6.7)$$

The key of this method is that both EL and PL are tested in the same geometry, so that the out-coupling efficiency,  $\eta_{OC}$ , which is often difficult to measure, could be

canceled out, and from which an expression for spin fraction  $\chi$ , can be reached as in Equation (6.8). Here  $P_{EL}$  and  $I_{inj}$  are the EL power and injected current at forward bias with the same setup.

$$\chi = \frac{\eta_{EQE}}{\eta_{OC}\eta_{PLY}} = \frac{P_{EL}}{I_{inj}} / \frac{-\Delta P_{PL}}{I_{ph}} \quad (6.8)$$

Preliminary measurement on spin fraction had already been done by Dr. Kai-Yuan Cheng in our group before. However, as the hole transport material (poly-TPD) had a bandgap of 2.8 eV, which could absorb significantly amount of incident laser photons, Dr. Cheng simply removed that layer and conducted the experiment at DC bias. Assuming a unity value for  $\gamma$ , the corresponding  $\chi$  was estimated to be ~56%.

Although this number is lower than the calculated value previously, it proves that more than 25% of the total excitons could radiate in our SiNC-OLEDs. But there are still two problems associated with his experiment. First, the device efficiency is not optimized because of lack of hole transport layer. Thus  $\gamma$  may deviate significantly from unity. Second, leakage current under reverse bias is not taken into consideration. This will lead to an overestimation of photocurrent.

To solve the first problem, a new device structure is proposed. Here we will use Poly(9-vinylcarbazole), or PVK, to replace low bandgap hole transport material poly-TPD, which helps confine the excitons in the SiNC layer without absorbing 405 nm laser photons. The energy band diagram is shown in Figure 6.3. However, PVK is known to be redissolved by chloroform when spin-coating SiNC solution, so that device performance is poor [36]. To prevent redissolving, we propose to insert a thin layer of wide bandgap optically transparent Nickel Oxide (NiO) in the middle. The matched energy levels and

much higher mobility will not greatly shift the exciton recombination zone, so that high EQE could still be achieved.

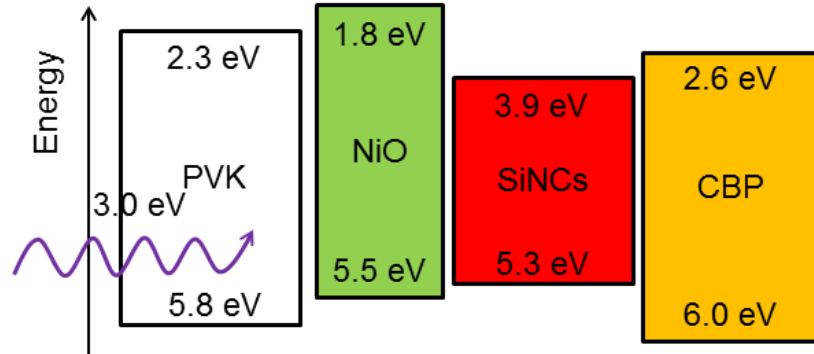


Figure 6.3 Energy band diagram of proposed device structure for spin fraction measurement.

The leakage current at reverse DC bias could be screened out with the two-tone synchronous measurement setup as shown in Figure 6.2. The 405 nm CW laser is cut by a mechanical chopper with frequency  $\omega_L$ , which also serves as a reference signal to measure photocurrent. Using a lock-in amplifier, the leakage current, which is in frequency  $\omega_B$ , will be discarded. Similarly, the voltage source working at frequency  $\omega_B$ , can also be used as a reference for the optical power. This experiment allows accurately probing the spin fraction in SiNCs.

### 6.3.2 Possible Mechanisms for High Spin Fraction

One possible mechanism that can raise the excitonic spin fraction up to unity is thermally activated delayed fluorescence (TADF), through which the lower energy triplet ( $T_1$ ) excitons can absorb a phonon from ambient and upconvert into higher energy singlets ( $S_1$ ). This process, so-called reverse intersystem crossing (RISC), can be better understood with the help of Figure 6.4. For a material with small energy difference ( $\Delta E_{ST}$ )

between  $S_1$  and  $T_1$  states, it is possible that the room ambient phonons could supply enough energy and momentum at the same time, which greatly facilitates this RISC transition. The non-radiative triplet excitons can thus be transformed into radiative singlets, and the total spin fraction  $\chi$  is increased.

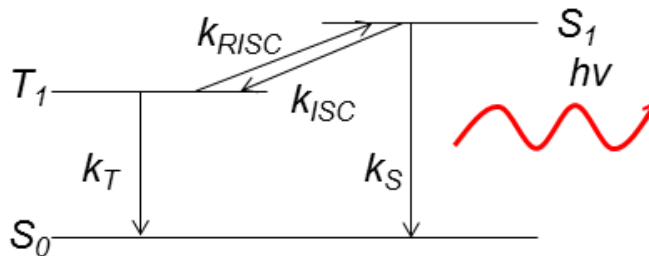


**Figure 6.4** Schematic plot of thermally activated delayed fluorescence (TADF).  $S_0$  is the ground state.  $T_1$  and  $S_1$  stand for triplet and singlet excited states;  $k_t$  and  $k_s$  represent triplet and single decay rates.  $k_{ISC}$  and  $k_{RISC}$  are inter-system crossing (ISC) and reverse intersystem crossing (RISC) rates, respectively.

In organic semiconductors, RISC is usually considered as a forbidden process. For instance, in the most frequently used phosphorescent chemical, Tris[2-phenylpyridinato-C2,N]iridium(III) ( $\text{Ir}(\text{ppy})_3$ ), the energy difference between  $S_1$  and  $T_1$  state ( $\Delta E_{ST}$ ) is about 850 meV [142]. The energy is much higher than room temperature phonon energy (25 meV) such that the phonon-assisted upconversion process becomes very unlikely.

However, TADF has recently been discovered in organic semiconductors (2,4,5,6-tetrakis(carbazol-9-yl)-1,3-dicyanobenzene (4CzIPN) [139] and 4,4',4''-Tris(N-3-methylphenyl-N-phenylamino)triphenylamine: 2-(4'-biphenyl)-5-4''-tert-butylphenyl)-1,3,4-oxadiazole mixture (m-MTDATA:t-Bu-PBD) [138] through carefully designing and modifying the energy levels. The OLEDs which utilized this mechanism reveal an EQE over 5%, the upper limit of common fluorescent OLEDs. The transient PL of this chemical, reveals a clear bi-exponential decay, with the pre-coefficient for the faster decay

component changing with temperature. This pre-coefficient also varies when the material is electrical excited instead of using laser pulse, as shown in Figure 6.5.

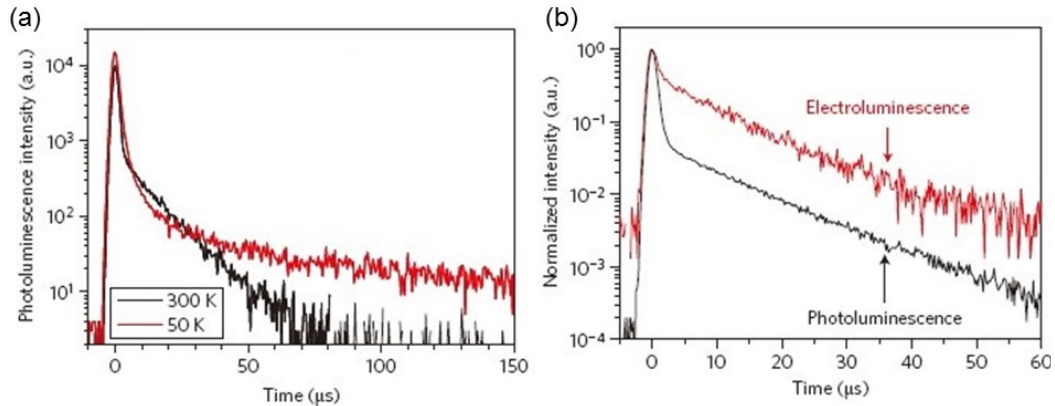


**Figure 6.5** Transient decay of 50 mol% m-MTDATA:t-Bu-PBD film. **(a)** transient PL at 300 K (black) and 50 K (red) and **(b)** comparison of PL (black) and EL (red) transient decay curve at 300 K. (Reprinted from [138])

While it is also possible for this process to happen in NC-OLEDs, no solid proof has been given. In CdSe NCs [60, 62] and porous Si [143], temperature dependent transient PL study have been conducted to support TADF mechanism. However, the authors to those papers simply take the total lifetime  $\tau$  as radiative lifetime  $\tau_r$  (in other words, assuming a unity value for  $\eta_{PL}$ ), which is problematic. Additionally, steady-state PL and transient EL experiments are in lack to validate TADF.

As argued earlier in this section, if the ambient phonon energy becomes not enough to support RISC at low temperature, integrated PL intensity will decrease significantly. However, within the temperature range (78 K to 296 K) in our PL experiments, this effect has not been observed. One possible reason is that ( $\Delta E_{ST}$ ) is typically smaller than 5 meV (corresponding to phonon energy at ~50 K) for SiNCs or porous Si [143]. To tell whether TADF happens or not, liquid Helium (~4 K) could be used for a complete temperature dependent PL and EL study.

Using the TADF schematic plot as shown in Figure 6.6, we are able to model the transient PL/EL decay process using Equation set (6.9) as shown below:

$$\begin{cases} \frac{dS_1}{dt} = R_1 - k_S S_1 - k_{ISC} S_1 + k_{RISC} T_1 \\ \frac{dT_1}{dt} = R_2 - k_T T_1 - k_{RISC} T_1 + k_{ISC} S_1 \end{cases} \quad (6.9)$$

In this equation set,  $R_1$  and  $R_2$  are the pump rate for  $S_1$  and  $T_1$  states, which become zero after the initial pulse. Solving Equation (6.9) will give the result as following:

$$\frac{d^2 S_1}{dt^2} + (k_S + k_{ISC} + k_T + k_{RISC}) \frac{dS_1}{dt} + (k_S k_T + k_S k_{RISC} + k_T k_{ISC}) S_1 = 0 \quad (6.10)$$

$$S_1(t) = A \exp(-t/t_1) + (1 - A) \exp(-t/t_2) \quad (6.11)$$

$$t_{1,2}^{-1} = \frac{k_S + k_T + k_{ISC} + k_{RISC} \pm \sqrt{(k_S + k_T + k_{ISC} + k_{RISC})^2 - 4(k_S k_{RISC} + k_T k_{ISC} + k_T k_S)}}{2} \quad (6.12)$$

Here  $t_{1,2}^{-1}$  are the two Eigen roots of Equation (6.10). If we choose  $t_1 < t_2$ ,  $A$  is precoefficient for the faster decay. These three terms could be obtained by fitting the transient decay curve  $S_1(t)$  with a bi-exponential.

To characterize the temperature dependence, we assume that the RISC process is thermally activated, the rate of which follows:

$$k_{RISC} = \begin{cases} k_{ISC} & \Delta E_{ST} < k_B T \\ k_{ISC} \exp\left(-\frac{\Delta E_{ST}}{k_B T}\right) & \Delta E_{ST} \geq k_B T \end{cases} \quad (6.13)$$

Note that ISC in organic semiconductors is usually a much faster process than singlet or triplet decay [99]. So at high temperature where  $\Delta E_{ST} \geq k_B T$ ,  $S_1$  and  $T_1$  states will essentially mix and the transient decay curve should reduce to a single exponential, as showed previously in Chapter 5.

In addition, boundary conditions of  $T_I$  should also be considered, as displayed in Equation (6.14). Combining Equation (6.9) to (6.14) could allow fitting for the value for  $\Delta E_{ST}$ .

$$T_1(0) = -\frac{A}{t_1} - \frac{1-A}{t_2} + k_S + k_{ISC} = 0 \text{ (PL) or } 3 \text{ (EL)} \quad (6.14)$$

To sum this section, future work on temperature dependent transient PL and EL study will be helpful to determine whether TADF is the mechanism for high spin fraction in our SiNC-OLEDs.

## 6.4 Energy Transfer in Silicon Nanocrystals

Energy transfer process is an important process that impacts on exciton spin fraction in OLEDs [91, 135] and NC-OLEDs [43]. In phosphorescent OLEDs, such process is a necessary requirement to reach nearly unity spin fraction [136]. In term of CdSe NCs, evidence has also been given for possible exciton transfer from phosphors [47].

There are mainly two types of energy transfer process in organic semiconductors, Förster energy transfer [144] and Dexter energy transfer [145]. The former depends significantly on the spectral overlap between absorption and emission. This process is based on the Coulombic interaction, or dipole-dipole mediated mechanism, as shown in Figure 6.6 (a). It can be easily understood as transition of energy between donor and acceptor, but without emission of photon. Dexter energy transfer, on the other hand, is a short-ranged process, which depends on the collision of electron clouds. For this process to happen, significant overlap of electron clouds of donor and acceptor in real space is required, as envisioned in Figure 6.6 (b). Note that the effective range is 5 ~ 10 nm for

Förster process but only  $\sim 1$  nm for Dexter process. So at long range, Dexter process is frequently ignored [146].

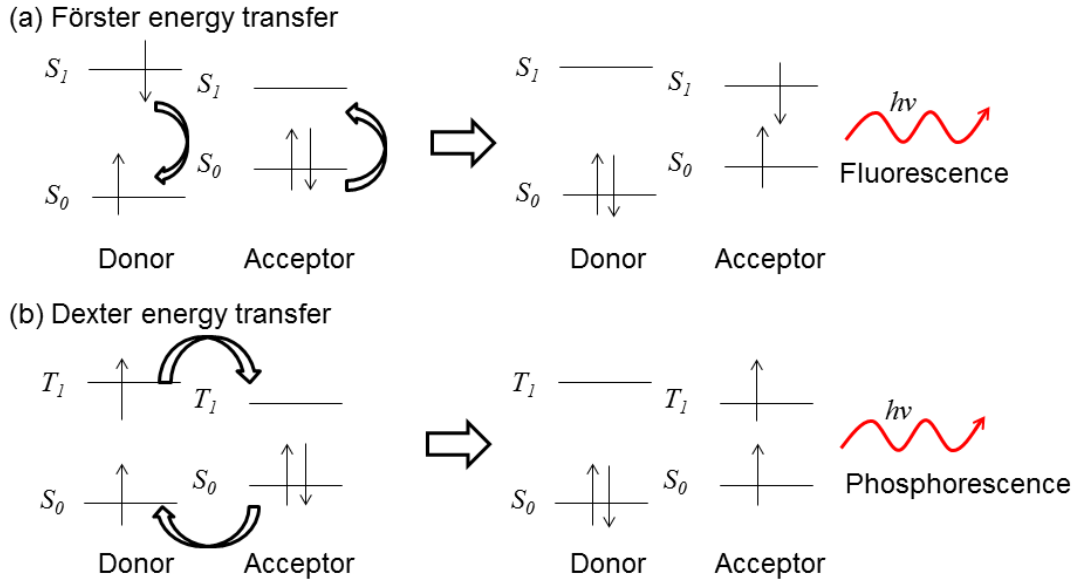


**Figure 6.8** Schematic diagram of two energy transfer processes: **(a)** Förster energy transfer and **(b)** Dexter energy transfer. The arrows represent electrons with spin direction either upward or downward.

Here we are interested to explore whether such process happens or even is responsible for the high spin fraction in our SiNC-OLEDs or not. In our previous design using Poly[2-methoxy-5-(2-ethylhexyloxy)-1,4-phenylenevinylene] (MEH-PPV, with a 2.1 eV bandgap) as hole transport material, due to little spectral overlap between SiNCs absorption and MEH-PPV emission, exciton transfer is very unlikely [33]. But the situation becomes different for poly-TPD (bandgap 2.8 eV) [34]. The spectral overlap is greatly enhanced thus the possibility of exciton transfer cannot be ignored.

It should be mentioned that in some conjugated polymer semiconductors, probably due to electron and hole exchange interaction, exciton spin fraction is shown to be higher

than the 25% limit [141]. If it is also true for poly-TPD, spin fraction of our SiNC-OLEDs could also be affected.

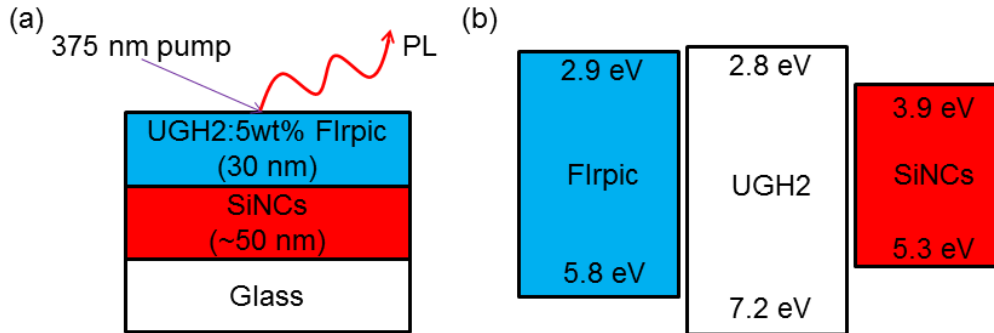


**Figure 6.7** (a) Proposed PL quenching geometry and (b) energy levels of materials involved in the PL quenching experiment.

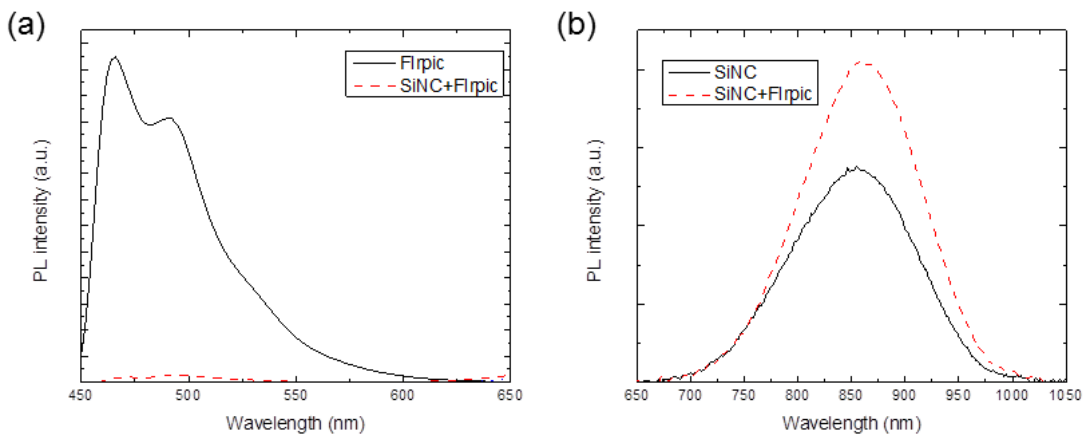


**Figure 6.8** (a) Comparison of pure Flrpic (black solid) and SiNC+Flrpic (red dash) PL spectra. (b) Comparison of pure SiNC (black solid) and SiNC+Flrpic (red dash) PL spectra.

To test existence of exciton transfer in SiNCs, for an initial try, we design a PL quenching experiment as shown in Figure 6.7 (a). Bis[2-(4,6-difluorophenyl)pyridinato-C2,N](picolinato)iridium(III) (Flrpic) is selected because it demonstrates a similar bandgap (2.9 eV) with poly-TPD but with much higher  $\eta_{PL}$  ( $\sim 90\%$ , instead of 10%). Interestingly, we find that when SiNCs layer is deposited underneath Flrpic, the emission due to Flrpic is greatly quenched. Meanwhile, compared to pure SiNC, emission in the

near infrared spectrum is significantly enhanced when FIRpic is used, as shown in Figure 6.8. This trial suggests that exciton transfer may happen efficiently between FIRpic and SiNCs.

In order to model this process, we follow the model described in [146]. We here consider only Förster process since Dexter process is short-ranged. The effective transfer range, or Förster radius  $R_0$ , is given by Equation (6.15) [99]:

$$R_0^6 = \frac{9\eta_{PL}\kappa^2}{128\pi^5 n^4} \int \lambda^4 F_d(\lambda) \sigma_A(\lambda) d\lambda \quad (6.15)$$

In this equation,  $\kappa$  is the dipole orientation factor and  $n$  is the refractive index.  $F_d(\lambda)$  and  $\sigma_A(\lambda)$  stand for the normalized donor emission and acceptor absorption cross-section spectra, respectively.

In a thick quenching layer geometry, the exciton transfer rate,  $k_F(d)$ , is given by Equation (6.16) [147]:

$$k_F(d) = \frac{\rho_A \pi R_0^6}{\tau 6d^3} \quad (6.16)$$

Where  $\rho_A$  is the molecular density of acceptor,  $\tau$  is exciton lifetime and  $d$  is the distance between donor and acceptor.

Taking exciton transfer as an additional term in one dimension diffusion equation, we can thus have:

$$D \frac{d^2 n(x)}{dx^2} - \frac{n(x)}{\tau} + \frac{Q(x)}{h\nu} - n(x)k_F(d) = 0 \quad (6.17)$$

In Equation (6.17),  $D$  is the diffusion coefficient,  $n(x)$  is the concentration function, and  $Q(x)$  is the generation profile of excitons. We can easily change the donor-acceptor distance,  $d$ , by inserting an optical transparent layer, triphenyl-(4-triphenylsilylphenyl)silane (UGH2, bandgap 4.4 eV), in the middle, as shown in Figure

6.9 (b). This allows numerically fitting for Förster radius  $R_0$ . A large value of  $R_0$  could suggest efficient energy transfer. Experiment with poly-TPD and SiNCs will be conducted later.

## **6.5 Afterword**

In the last two decades, significant improvement on device efficiency in NC-OLEDs has been made. We hope that through this study, electrical and optical properties of SiNCs could be connected adequately to their device performance. Of course, more research is needed to be done to elucidate the exciton spin fraction in SiNCs, and to realize of long-lifetime and full-color-display for future commercialization. This work may serve as a useful guidance to help select and synthesize proper NCs, and design highly efficient NC based optoelectronic devices in the future.

## References:

- [1] L. Brus, "Electronic wave functions in semiconductor clusters: experiment and theory," *The Journal of Physical Chemistry*, vol. 90, pp. 2555-2560, 1986.
- [2] B. Delley and E. F. Steigmeier, "Quantum confinement in Si nanocrystals," *Physical Review B*, vol. 47, pp. 1397-1400, 1993.
- [3] C. Murray, D. Norris, and M. G. Bawendi, "Synthesis and characterization of nearly monodisperse CdE (E= sulfur, selenium, tellurium) semiconductor nanocrystallites," *Journal of the American Chemical Society*, vol. 115, pp. 8706-8715, 1993.
- [4] R. Tsu, L. Ioriatti, J. F. Harvey, H. Shen, and R. A. Lux, "Quantum confinement effects on the dielectric constant of porous silicon," 1993, pp. 437-440.
- [5] Y. M. Niquet, G. Allan, C. Delerue, and M. Lannoo, "Quantum confinement in germanium nanocrystals," *Applied Physics Letters*, vol. 77, pp. 1182-1184, 2000.
- [6] A. D. Yoffe, "Semiconductor quantum dots and related systems: Electronic, optical, luminescence and related properties of low dimensional systems," *Advances in Physics*, vol. 50, pp. 1-208, 2001.
- [7] M. Law, J. Goldberger, and P. Yang, "Semiconductor nanowires and nanotubes," vol. 34, ed, 2004, pp. 83-122.
- [8] A. M. Smith and S. Nie, "Semiconductor nanocrystals: Structure, properties, and band gap engineering," *Accounts of Chemical Research*, vol. 43, pp. 190-200, 2010.
- [9] G. Allan and C. Delerue, "Confinement effects in PbSe quantum wells and nanocrystals," *Physical Review B - Condensed Matter and Materials Physics*, vol. 70, pp. 1-9, 2004.
- [10] J. Heitmann, F. Müller, L. Yi, M. Zacharias, D. Kovalev, and F. Eichhorn, "Excitons in Si nanocrystals: confinement and migration effects," *Physical Review B*, vol. 69, p. 195309, 2004.
- [11] I. Moreels, K. Lambert, D. Smeets, D. De Muynck, T. Nollet, J. C. Martins, F. Vanhaecke, A. Vantomme, C. Delerue, G. Allan, and Z. Hens, "Size-dependent optical properties of colloidal PbS quantum dots," *ACS Nano*, vol. 3, pp. 3023-3030, 2009.

- [12] D. S. English, L. E. Pell, Z. Yu, P. F. Barbara, and B. A. Korgel, "Size Tunable Visible Luminescence from Individual Organic Monolayer Stabilized Silicon Nanocrystal Quantum Dots," *Nano Letters*, vol. 2, pp. 681-685, 2002.
- [13] A. Olkhovets, R. C. Hsu, A. Lipovskii, and F. W. Wise, "Size-dependent temperature variation of the energy gap in lead-salt quantum dots," *Physical review letters*, vol. 81, pp. 3539-3542, 1998.
- [14] T. Van Buuren, L. Dinh, L. Chase, W. Siekhaus, and L. J. Terminello, "Changes in the electronic properties of Si nanocrystals as a function of particle size," *Physical review letters*, vol. 80, pp. 3803-3806, 1998.
- [15] L. Bakueva, S. Musikhin, M. Hines, T.-W. Chang, M. Tzolov, G. Scholes, and E. Sargent, "Size-tunable infrared (1000–1600 nm) electroluminescence from PbS quantum-dot nanocrystals in a semiconducting polymer," *Applied Physics Letters*, vol. 82, pp. 2895-2897, 2003.
- [16] S. Kan, T. Mokari, E. Rothenberg, and U. Banin, "Synthesis and size-dependent properties of zinc-blende semiconductor quantum rods," *Nature Materials*, vol. 2, pp. 155-158, 2003.
- [17] M. Sykora, L. Mangolini, R. D. Schaller, U. Kortshagen, D. Jurbergs, and V. I. Klimov, "Size-dependent intrinsic radiative decay rates of silicon nanocrystals at large confinement energies," *Physical review letters*, vol. 100, p. 067401, 2008.
- [18] R. Anthony and U. Kortshagen, "Photoluminescence quantum yields of amorphous and crystalline silicon nanoparticles," *Physical Review B*, vol. 80, p. 115407, 2009.
- [19] D. V. Talapin, J.-S. Lee, M. V. Kovalenko, and E. V. Shevchenko, "Prospects of colloidal nanocrystals for electronic and optoelectronic applications," *Chemical Reviews*, vol. 110, pp. 389-458, 2009.
- [20] C. B. Murray, C. R. Kagan, and M. G. Bawendi, "Synthesis and characterization of monodisperse nanocrystals and close-packed nanocrystal assemblies," *Annual Review of Materials Science*, vol. 30, pp. 545-610, 2000.
- [21] S. Coe - Sullivan, J. S. Steckel, W. K. Woo, M. G. Bawendi, and V. Bulović, "Large - Area Ordered Quantum - Dot Monolayers via Phase Separation During Spin - Casting," *Advanced Functional Materials*, vol. 15, pp. 1117-1124, 2005.
- [22] I. Gur, N. A. Fromer, M. L. Geier, and A. P. Alivisatos, "Materials science: Air-stable all-inorganic nanocrystal solar cells processed from solution," *Science*, vol. 310, pp. 462-465, 2005.

- [23] D. V. Talapin and C. B. Murray, "PbSe nanocrystal solids for n-and p-channel thin film field-effect transistors," *Science*, vol. 310, pp. 86-89, 2005.
- [24] P. V. Kamat, "Quantum dot solar cells. Semiconductor nanocrystals as light harvesters," *Journal of Physical Chemistry C*, vol. 112, pp. 18737-18753, 2008.
- [25] G. M. Whitesides, "Nanoscience, nanotechnology, and chemistry," *Small*, vol. 1, pp. 172-179, 2005.
- [26] J. Aizenberg, J. C. Weaver, M. S. Thanawala, V. C. Sundar, D. E. Morse, and P. Fratzl, "Materials science: Skeleton of euplectella sp.: Structural hierarchy from the nanoscale to the macroscale," *Science*, vol. 309, pp. 275-278, 2005.
- [27] B. D. Gates, Q. Xu, M. Stewart, D. Ryan, C. G. Willson, and G. M. Whitesides, "New approaches to nanofabrication: Molding, printing, and other techniques," *Chemical Reviews*, vol. 105, pp. 1171-1196, 2005.
- [28] W. Lu and C. M. Lieber, "Nanoelectronics from the bottom up," *Nature Materials*, vol. 6, pp. 841-850, 2007.
- [29] N. C. Greenham, X. Peng, and A. P. Alivisatos, "Charge separation and transport in conjugated-polymer/semiconductor-nanocrystal composites studied by photoluminescence quenching and photoconductivity," *Physical Review B*, vol. 54, p. 17628, 1996.
- [30] K. W. Johnston, A. G. Pattantyus-Abraham, J. P. Clifford, S. H. Myrskog, S. Hoogland, H. Shukla, E. J. Klem, L. Levina, and E. H. Sargent, "Efficient Schottky-quantum-dot photovoltaics: The roles of depletion, drift, and diffusion," *Applied Physics Letters*, vol. 92, pp. 122111-122111-3, 2008.
- [31] J. M. Luther, M. Law, M. C. Beard, Q. Song, M. O. Reese, R. J. Ellingson, and A. J. Nozik, "Schottky solar cells based on colloidal nanocrystal films," *Nano Letters*, vol. 8, pp. 3488-3492, 2008.
- [32] M. G. Panthani, V. Akhavan, B. Goodfellow, J. P. Schmidtke, L. Dunn, A. Dodabalapur, P. F. Barbara, and B. A. Korgel, "Synthesis of CuInS<sub>2</sub>, CuInSe<sub>2</sub>, and Cu(In<sub>x</sub>Ga<sub>1-x</sub>)Se<sub>2</sub> (CIGS) nanocrystal "inks" for printable photovoltaics," *Journal of the American Chemical Society*, vol. 130, pp. 16770-16777, 2008.
- [33] K.-Y. Cheng, R. Anthony, U. R. Kortshagen, and R. J. Holmes, "Hybrid Silicon Nanocrystal–Organic Light-Emitting Devices for Infrared Electroluminescence," *Nano Letters*, vol. 10, pp. 1154-1157, 2010.

- [34] K. Y. Cheng, R. Anthony, U. R. Kortshagen, and R. J. Holmes, "High-efficiency silicon nanocrystal light-emitting devices," *Nano Lett*, vol. 11, pp. 1952-1956, 2011.
- [35] B. S. Mashford, M. Stevenson, Z. Popovic, C. Hamilton, Z. Zhou, C. Breen, J. Steckel, V. Bulovic, M. Bawendi, and S. Coe-Sullivan, "High-efficiency quantum-dot light-emitting devices with enhanced charge injection," *Nature Photonics*, 2013.
- [36] D. P. Puzzo, E. J. Henderson, M. G. Helander, Z. B. Wang, G. A. Ozin, and Z. Lu, "Visible colloidal nanocrystal silicon light-emitting diode," *Nano Lett*, vol. 11, pp. 1585-1590, 2011.
- [37] P. O. Anikeeva, J. E. Halpert, M. G. Bawendi, and V. Bulovic, "Quantum dot light-emitting devices with electroluminescence tunable over the entire visible spectrum," *Nano Lett*, vol. 9, pp. 2532-2536, 2009.
- [38] K. Bourdakos, D. Dissanayake, T. Lutz, S. Silva, and R. Curry, "Highly efficient near-infrared hybrid organic-inorganic nanocrystal electroluminescence device," *Applied Physics Letters*, vol. 92, pp. 153311-153311-3, 2008.
- [39] R. J. Walters, "Silicon nanocrystals for silicon photonics," California Institute of Technology, 2007.
- [40] R. J. Walters, G. I. Bourianoff, and H. A. Atwater, "Field-effect electroluminescence in silicon nanocrystals," *Nature Materials*, vol. 4, pp. 143-146, 2005.
- [41] N. Tessler, V. Medvedev, M. Kazes, S. Kan, and U. Banin, "Efficient near-infrared polymer nanocrystal light-emitting diodes," *Science*, vol. 295, pp. 1506-1508, 2002.
- [42] H. Kim, C. Gilmore, A. Pique, J. Horwitz, H. Mattoussi, H. Murata, Z. Kafafi, and D. Chrisey, "Electrical, optical, and structural properties of indium–tin–oxide thin films for organic light-emitting devices," *Journal of Applied Physics*, vol. 86, pp. 6451-6461, 1999.
- [43] V. Colvin, M. Schlamp, and A. Alivisatos, "Light-emitting diodes made from cadmium selenide nanocrystals and a semiconducting polymer," *Nature*, vol. 370, pp. 354-357, 1994.
- [44] S. V. Kershaw, M. T. Harrison, and M. G. Burt, "Putting nanocrystals to work: from solutions to devices," *Philosophical Transactions of the Royal Society of*

*London. Series A: Mathematical, Physical and Engineering Sciences*, vol. 361, pp. 331-343, 2003.

- [45] R. Friend, R. Gymer, A. Holmes, J. Burroughes, R. Marks, C. Taliani, D. Bradley, D. Dos Santos, J. Bredas, and M. Lögdlund, "Electroluminescence in conjugated polymers," *Nature*, vol. 397, pp. 121-128, 1999.
- [46] J. S. Steckel, S. Coe - Sullivan, V. Bulović, and M. G. Bawendi, "1.3  $\mu\text{m}$  to 1.55  $\mu\text{m}$  tunable electroluminescence from PbSe quantum dots embedded within an organic device," *Advanced Materials*, vol. 15, pp. 1862-1866, 2003.
- [47] P. Anikeeva, C. Madigan, S. Coe-Sullivan, J. Steckel, M. Bawendi, and V. Bulović, "Photoluminescence of CdSe/ZnS core/shell quantum dots enhanced by energy transfer from a phosphorescent donor," *Chemical physics letters*, vol. 424, pp. 120-125, 2006.
- [48] P. O. Anikeeva, J. E. Halpert, M. G. Bawendi, and V. Bulovic, "Electroluminescence from a mixed red-green-blue colloidal quantum dot monolayer," *Nano Lett*, vol. 7, pp. 2196-2200, 2007.
- [49] M. J. Panzer, V. Wood, S. M. Geyer, M. G. Bawendi, and V. Bulović, "Tunable Infrared Emission From Printed Colloidal Quantum Dot/Polymer Composite Films on Flexible Substrates," *Journal of display technology*, vol. 6, pp. 90-93, 2010.
- [50] P. Avouris, Z. Chen, and V. Perebeinos, "Carbon-based electronics," *Nature nanotechnology*, vol. 2, pp. 605-615, 2007.
- [51] B. Landi, S. Castro, H. Ruf, C. Evans, S. Bailey, and R. Raffaele, "CdSe quantum dot-single wall carbon nanotube complexes for polymeric solar cells," *Solar Energy Materials and Solar Cells*, vol. 87, pp. 733-746, 2005.
- [52] X. Peng, J. Chen, J. A. Misewich, and S. S. Wong, "Carbon nanotube–nanocrystal heterostructures," *Chemical Society Reviews*, vol. 38, pp. 1076-1098, 2009.
- [53] S. Banerjee and S. S. Wong, "Synthesis and characterization of carbon nanotube–nanocrystal heterostructures," *Nano Lett*, vol. 2, pp. 195-200, 2002.
- [54] H. Huang, C. Liu, Y. Wu, and S. Fan, "Aligned carbon nanotube composite films for thermal management," *Advanced materials*, vol. 17, pp. 1652-1656, 2005.
- [55] X. Duan, C. Niu, V. Sahi, J. Chen, J. W. Parce, S. Empedocles, and J. L. Goldman, "High-performance thin-film transistors using semiconductor nanowires and nanoribbons," *Nature*, vol. 425, pp. 274-278, 2003.

- [56] S. Srivastava and N. A. Kotov, "Composite layer-by-layer (LBL) assembly with inorganic nanoparticles and nanowires," *Accounts of chemical research*, vol. 41, pp. 1831-1841, 2008.
- [57] W. Feng, L.-D. Sun, and C.-H. Yan, "Ag nanowires enhanced upconversion emission of NaYF<sub>4</sub>: Yb, Er nanocrystals via a direct assembly method," *Chem. Commun.*, pp. 4393-4395, 2009.
- [58] K. S. Leschkies, R. Divakar, J. Basu, E. Enache-Pommer, J. E. Boercker, C. B. Carter, U. R. Kortshagen, D. J. Norris, and E. S. Aydil, "Photosensitization of ZnO nanowires with CdSe quantum dots for photovoltaic devices," *Nano Lett*, vol. 7, pp. 1793-1798, 2007.
- [59] R. Hikmet, D. Talapin, and H. Weller, "Study of conduction mechanism and electroluminescence in CdSe/ZnS quantum dot composites," *Journal of Applied Physics*, vol. 93, pp. 3509-3514, 2003.
- [60] S. Crooker, T. Barrick, J. Hollingsworth, and V. Klimov, "Multiple temperature regimes of radiative decay in CdSe nanocrystal quantum dots: Intrinsic limits to the dark-exciton lifetime," *Applied Physics Letters*, vol. 82, pp. 2793-2795, 2003.
- [61] D. Valerini, A. Creti, M. Lomascolo, L. Manna, R. Cingolani, and M. Anni, "Temperature dependence of the photoluminescence properties of colloidal CdSe / ZnS core/shell quantum dots embedded in a polystyrene matrix," *Physical Review B*, vol. 71, p. 235409, 2005.
- [62] M. Califano, A. Franceschetti, and A. Zunger, "Temperature dependence of excitonic radiative decay in CdSe quantum dots: The role of surface hole traps," *Nano Letters*, vol. 5, pp. 2360-2364, 2005.
- [63] P. Jing, J. Zheng, M. Ikezawa, X. Liu, S. Lv, X. Kong, J. Zhao, and Y. Masumoto, "Temperature-dependent photoluminescence of CdSe-core CdS/CdZnS/ZnS-multishell quantum dots," *The Journal of Physical Chemistry C*, vol. 113, pp. 13545-13550, 2009.
- [64] J. M. Elward and A. Chakraborty, "Effect of dot size on exciton binding energy and electron-hole recombination probability in CdSe quantum dots," *arXiv preprint arXiv:1306.2110*, 2013.
- [65] B. Dabbousi, J. Rodriguez-Viejo, F. V. Mikulec, J. Heine, H. Mattoussi, R. Ober, K. Jensen, and M. Bawendi, "(CdSe) ZnS core-shell quantum dots: synthesis and characterization of a size series of highly luminescent nanocrystallites," *The Journal of Physical Chemistry B*, vol. 101, pp. 9463-9475, 1997.

- [66] W. L. Ng, M. Lourenco, R. Gwilliam, S. Ledain, G. Shao, and K. Homewood, "An efficient room-temperature silicon-based light-emitting diode," *Nature*, vol. 410, pp. 192-194, 2001.
- [67] C. Kittel and P. McEuen, *Introduction to solid state physics* vol. 7: Wiley New York, 1996.
- [68] C. Meier, A. Gondorf, S. Luttjohann, A. Lorke, and H. Wiggers, "Silicon nanoparticles: Absorption, emission, and the nature of the electronic bandgap," *Journal of Applied Physics*, vol. 101, pp. 103112-103112-8, 2007.
- [69] X. D. Pi, R. W. Liptak, J. D. Nowak, N. P. Wells, C. B. Carter, S. A. Campbell, and U. Kortshagen, "Air-stable full-visible-spectrum emission from silicon nanocrystals synthesized by an all-gas-phase plasma approach," *Nanotechnology*, vol. 19, p. 245603, 2008.
- [70] B. Hoefflinger, "ITRS: The International Technology Roadmap for Semiconductors," in *Chips 2020*, ed: Springer, 2012, pp. 161-174.
- [71] V. I. Klimov, *Semiconductor and metal nanocrystals: synthesis and electronic and optical properties*: CRC Press, 2003.
- [72] A. Yoffe, "Low-dimensional systems: quantum size effects and electronic properties of semiconductor microcrystallites (zero-dimensional systems) and some quasi-two-dimensional systems," *Advances in Physics*, vol. 51, pp. 799-890, 2002.
- [73] M. C. Beard, K. P. Knutsen, P. Yu, J. M. Luther, Q. Song, W. K. Metzger, R. J. Ellingson, and A. J. Nozik, "Multiple exciton generation in colloidal silicon nanocrystals," *Nano Lett*, vol. 7, pp. 2506-2512, 2007.
- [74] A. P. Alivisatos, "Perspectives on the physical chemistry of semiconductor nanocrystals," *The Journal of Physical Chemistry*, vol. 100, pp. 13226-13239, 1996.
- [75] P. C. Hiemenz and R. Rajagopalan, *Principles of Colloid and Surface Chemistry, revised and expanded* vol. 14: CRC Press, 1997.
- [76] L. E. Brus, "Electron - electron and electron - hole interactions in small semiconductor crystallites: The size dependence of the lowest excited electronic state," *The journal of chemical physics*, vol. 80, p. 4403, 1984.

- [77] K. Y. Cheng, R. Anthony, U. R. Kortshagen, and R. J. Holmes, "Hybrid Silicon Nanocrystal– Organic Light-Emitting Devices for Infrared Electroluminescence," *Nano Lett*, vol. 10, pp. 1154-1157, 2010.
- [78] R. H. Parmenter and W. Ruppel, "Two - Carrier Space - Charge - Limited Current in a Trap - Free Insulator," *Journal of Applied Physics*, vol. 30, pp. 1548-1558, 1959.
- [79] J. Frenkel, "On pre-breakdown phenomena in insulators and electronic semi-conductors," *Physical Review*, vol. 54, p. 647, 1938.
- [80] W. Shockley and W. Read Jr, "Statistics of the recombinations of holes and electrons," *Physical Review*, vol. 87, p. 835, 1952.
- [81] D. Kovalev, H. Heckler, M. Ben-Chorin, G. Polisski, M. Schwartzkopff, and F. Koch, "Breakdown of the k-conservation rule in Si nanocrystals," *Physical review letters*, vol. 81, pp. 2803-2806, 1998.
- [82] G. M. Credo, M. D. Mason, and S. K. Buratto, "External quantum efficiency of single porous silicon nanoparticles," *Applied Physics Letters*, vol. 74, pp. 1978-1980, 1999.
- [83] C. Delerue, G. Allan, C. Reynaud, O. Guillois, G. Ledoux, and F. Huisken, "Multiexponential photoluminescence decay in indirect-gap semiconductor nanocrystals," *Physical Review B*, vol. 73, p. 235318, 2006.
- [84] H. E. Roman and L. Pavesi, "Monte Carlo simulations of the recombination dynamics in porous silicon," *Journal of Physics: Condensed Matter*, vol. 8, p. 5161, 1999.
- [85] S. Pimputkar, J. S. Speck, S. P. DenBaars, and S. Nakamura, "Prospects for LED lighting," *Nature Photonics*, vol. 3, pp. 180-182, 2009.
- [86] N. Zheludev, "The life and times of the LED—a 100-year history," *Nature Photonics*, vol. 1, pp. 189-192, 2007.
- [87] C. Tang and S. VanSlyke, "Organic electroluminescent diodes," *Applied Physics Letters*, vol. 51, p. 913, 1987.
- [88] P. O. Anikeeva, J. E. Halpert, M. G. Bawendi, and V. Bulovic, "Quantum dot light-emitting devices with electroluminescence tunable over the entire visible spectrum," *Nano Letters*, vol. 9, pp. 2532-2536, 2009.

- [89] S. Coe, W.-K. Woo, V. B. Mounji Bawendi, and cacute, "Electroluminescence from single monolayers of nanocrystals in molecular organic devices," *Nature*, vol. 420, pp. 800-803, 2002.
- [90] X. Ma, F. Xu, J. Benavides, and S. G. Cloutier, "High performance hybrid near-infrared LEDs using benzenedithiol cross-linked PbS colloidal nanocrystals," *Organic Electronics*, vol. 13, pp. 525-531, 2012.
- [91] M. Baldo, D. O'brien, Y. You, A. Shoustikov, S. Sibley, M. Thompson, and S. Forrest, "Highly efficient phosphorescent emission from organic electroluminescent devices," *Nature*, vol. 395, pp. 151-154, 1998.
- [92] R. Weissleder, "A clearer vision for in vivo imaging," *Nature biotechnology*, vol. 19, pp. 316-316, 2001.
- [93] Y. T. Lim, S. Kim, A. Nakayama, N. E. Stott, M. G. Bawendi, and J. V. Frangioni, "Selection of quantum dot wavelengths for biomedical assays and imaging," *Molecular Imaging*, vol. 2, pp. 50-64, 2003.
- [94] S. Kim, Y. T. Lim, E. G. Soltész, A. M. De Grand, J. Lee, A. Nakayama, J. A. Parker, T. Mihaljevic, R. G. Laurence, and D. M. Dor, "Near-infrared fluorescent type II quantum dots for sentinel lymph node mapping," *Nature biotechnology*, vol. 22, pp. 93-97, 2003.
- [95] L. Sun, J. J. Choi, D. Stachnik, A. C. Bartnik, B.-R. Hyun, G. G. Malliaras, T. Hanrath, and F. W. Wise, "Bright infrared quantum-dot light-emitting diodes through inter-dot spacing control," *Nature nanotechnology*, vol. 7, pp. 369-373, 2012.
- [96] L. Canham, "Silicon quantum wire array fabrication by electrochemical and chemical dissolution of wafers," *Applied Physics Letters*, vol. 57, pp. 1046-1048, 1990.
- [97] K. Hong and J. L. Lee, "Review paper: Recent developments in light extraction technologies of organic light emitting diodes," *Electronic Materials Letters*, vol. 7, pp. 77-91, 2011.
- [98] A. E. Farghal, S. M. Wageh, and A. E.-S. Abou-El-Azm, "Electromagnetic modeling of outcoupling efficiency and light emission in near-infrared quantum dot light emitting devices," *Progress In Electromagnetics Research B*, vol. 24, pp. 263-284, 2010.
- [99] N. J. Turro, *Modern molecular photochemistry*: Univ Science Books, 1991.

- [100] L. Mangolini, E. Thimsen, and U. Kortshagen, "High-yield plasma synthesis of luminescent silicon nanocrystals," *Nano Letters*, vol. 5, pp. 655-659, 2005.
- [101] J. M. Buriak, "Organometallic Chemistry on Silicon and Germanium Surfaces," *Chemical Reviews*, vol. 102, pp. 1271-1308, 2002/05/01 2002.
- [102] M. S. Kang, A. Sahu, D. J. Norris, and C. D. Frisbie, "Size-dependent electrical transport in CdSe nanocrystal thin films," *Nano Lett*, vol. 10, pp. 3727-3732, 2010.
- [103] Z. C. Holman, C. Y. Liu, and U. R. Kortshagen, "Germanium and silicon nanocrystal thin-film field-effect transistors from solution," *Nano Lett*, vol. 10, pp. 2661-6, Jul 14 2010.
- [104] T. Mentzel, V. Porter, S. Geyer, K. MacLean, M. G. Bawendi, and M. Kastner, "Charge transport in PbSe nanocrystal arrays," *Physical Review B*, vol. 77, p. 075316, 2008.
- [105] D. Ginger and N. Greenham, "Charge injection and transport in films of CdSe nanocrystals," *Journal of Applied Physics*, vol. 87, pp. 1361-1368, 2000.
- [106] D. Ginger and N. Greenham, "Charge transport in semiconductor nanocrystals," *Synthetic metals*, vol. 124, pp. 117-120, 2001.
- [107] P. Manousiadis, S. Gardelis, and A. Nassiopoulou, "Lateral electrical transport and photocurrent in single and multilayers of two-dimensional arrays of Si nanocrystals," *Journal of Applied Physics*, vol. 112, pp. 043704-043704-6, 2012.
- [108] M. Rafiq, Y. Tsuchiya, H. Mizuta, S. Oda, S. Uno, Z. Durrani, and W. Milne, "Charge injection and trapping in silicon nanocrystals," *Applied Physics Letters*, vol. 87, pp. 182101-182101-3, 2005.
- [109] M. Rafiq, Y. Tsuchiya, H. Mizuta, S. Oda, S. Uno, Z. Durrani, and W. Milne, "Hopping conduction in size-controlled Si nanocrystals," *Journal of Applied Physics*, vol. 100, pp. 014303-014303-4, 2006.
- [110] R. Hill, "The Poole-Frenkel constant," *Thin Solid Films*, vol. 8, p. 21, 1971.
- [111] A. K. Jonscher, "Electronic properties of amorphous dielectric films," *Thin Solid Films*, vol. 1, pp. 213-234, 1967.
- [112] A. Watt, T. Eichmann, H. Rubinsztein-Dunlop, and P. Meredith, "Carrier transport in PbS nanocrystal conducting polymer composites," *Applied Physics Letters*, vol. 87, pp. 1-3, 2005.

- [113] M. Ando, T. Kobayashi, H. Naito, T. Nagase, and Y. Kanemitsu, "Transient photocurrent of (silicon nanocrystals)-(organic polysilane) composites-detection of surface states of silicon nanocrystals," *Thin Solid Films*, vol. 499, pp. 119-122, 2006.
- [114] E. Couderc, N. Bruyant, A. Fiore, F. Chandezon, D. Djurado, P. Reiss, and J. Faure-Vincent, "Charge transport in poly(3-hexylthiophene):CdSe nanocrystals hybrid thin films investigated with time-of-flight measurements," *Applied Physics Letters*, vol. 101, 2012.
- [115] H. Scher and E. W. Montroll, "Anomalous transit-time dispersion in amorphous solids," *Physical Review B*, vol. 12, p. 2455, 1975.
- [116] N. Matsusue, Y. Suzuki, and H. Naito, "Charge carrier transport in red electrophosphorescent emitting layer," *Japanese journal of applied physics*, vol. 45, p. 5966, 2006.
- [117] J.-W. Kang, S.-H. Lee, H.-D. Park, W.-I. Jeong, K.-M. Yoo, Y.-S. Park, and J.-J. Kim, "Low roll-off of efficiency at high current density in phosphorescent organic light emitting diodes," *Applied Physics Letters*, vol. 90, pp. 223508-223508-3, 2007.
- [118] M. L. Mastronardi, F. Hennrich, E. J. Henderson, F. Maier-Flaig, C. Blum, J. Reichenbach, U. Lemmer, C. Kübel, D. Wang, M. M. Kappes, and G. A. Ozin, "Preparation of monodisperse silicon nanocrystals using density gradient ultracentrifugation," *Journal of the American Chemical Society*, vol. 133, pp. 11928-11931, 2011.
- [119] D. C. Hannah, J. Yang, P. Podsiadlo, M. K. Chan, A. Demortière, D. J. Gosztola, V. B. Prakapenka, G. C. Schatz, U. Kortshagen, and R. D. Schaller, "On the origin of photoluminescence in silicon nanocrystals: Pressure-dependent structural and optical studies," *Nano Letters*, vol. 12, pp. 4200-4205, 2012.
- [120] M. V. Wolkin, J. Jorne, P. M. Fauchet, G. Allan, and C. Delerue, "Electronic states and luminescence in porous silicon quantum dots: The role of oxygen," *Physical review letters*, vol. 82, pp. 197-200, 1999.
- [121] S. Godefroo, M. Hayne, M. Jivanescu, A. Stesmans, M. Zacharias, O. Lebedev, G. Van Tendeloo, and V. V. Moshchalkov, "Classification and control of the origin of photoluminescence from Si nanocrystals," *Nature nanotechnology*, vol. 3, pp. 174-178, 2008.

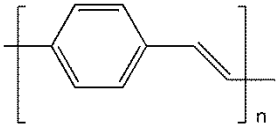
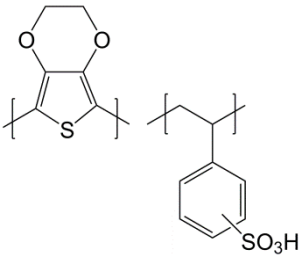
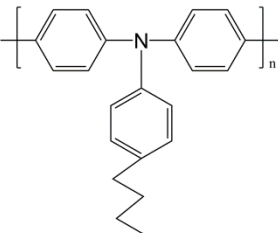
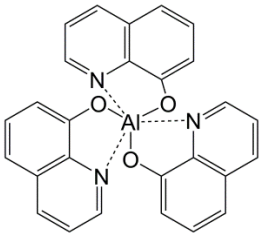
- [122] J. Linnros, N. Lalic, A. Galeckas, and V. Grivickas, "Analysis of the stretched exponential photoluminescence decay from nanometer-sized silicon crystals in SiO<sub>2</sub>," *Journal of Applied Physics*, vol. 86, pp. 6128-6134, 1999.
- [123] M. Dovrat, Y. Goshen, J. Jedrzejewski, I. Balberg, and A. Sa'Ar, "Radiative versus nonradiative decay processes in silicon nanocrystals probed by time-resolved photoluminescence spectroscopy," *Physical Review B*, vol. 69, p. 155311, 2004.
- [124] F. Trojánek, K. Neudert, M. Bittner, and P. Malý, "Picosecond photoluminescence and transient absorption in silicon nanocrystals," *Physical Review B*, vol. 72, p. 075365, 2005.
- [125] R. Walters, J. Kalkman, A. Polman, H. Atwater, and M. De Dood, "Photoluminescence quantum efficiency of dense silicon nanocrystal ensembles in SiO<sub>2</sub>," *Physical Review B*, vol. 73, p. 132302, 2006.
- [126] J. Carreras, J. Arbiol, B. Garrido, C. Bonafos, and J. Montserrat, "Direct modulation of electroluminescence from silicon nanocrystals beyond radiative recombination rates," *Applied Physics Letters*, vol. 92, pp. 091103-091103-3, 2008.
- [127] F. Maier-Flaig, E. J. Henderson, S. Valouch, S. Klinkhammer, C. Kübel, G. A. Ozin, and U. Lemmer, "Photophysics of organically-capped silicon nanocrystals—A closer look into silicon nanocrystal luminescence using low temperature transient spectroscopy," *Chemical Physics*, 2012.
- [128] R. J. Walters, J. Kalkman, A. Polman, H. A. Atwater, and M. J. A. De Dood, "Photoluminescence quantum efficiency of dense silicon nanocrystal ensembles in Si O<sub>2</sub>," *Physical Review B - Condensed Matter and Materials Physics*, vol. 73, 2006.
- [129] P. Calcott, K. Nash, L. Canham, M. Kane, and D. Brumhead, "Spectroscopic identification of the luminescence mechanism of highly porous silicon," *Journal of luminescence*, vol. 57, pp. 257-269, 1993.
- [130] D. C. Hannah, J. Yang, P. Podsiadlo, M. K. Y. Chan, A. Demortiere, D. J. Gosztola, V. B. Prakapenka, G. C. Schatz, U. R. Kortshagen, and R. D. Schaller, "On the Origin of Photoluminescence in Silicon Nanocrystals: Pressure-Dependent Structural and Optical Studies," *Nano Lett*, 2012.
- [131] Y. Varshni, "Temperature dependence of the energy gap in semiconductors," *Physica*, vol. 34, pp. 149-154, 1967.

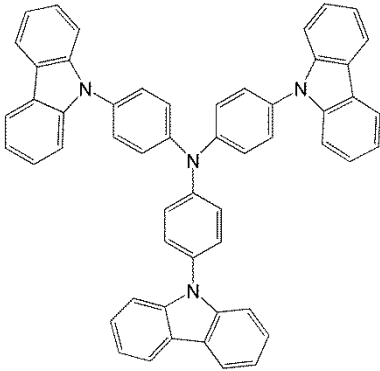
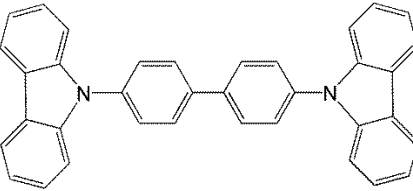
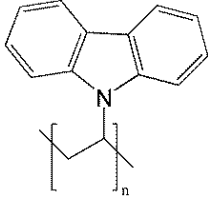
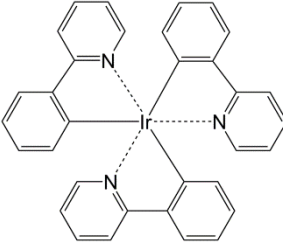
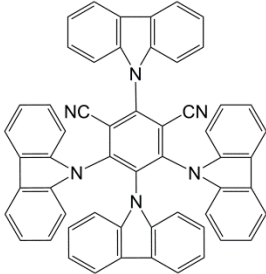
- [132] K. Lyon, G. Salinger, C. Swenson, and G. White, "Linear thermal expansion measurements on silicon from 6 to 340 K," *Journal of applied physics*, vol. 48, pp. 865-868, 1977.
- [133] K. Odonnell and X. Chen, "Temperature dependence of semiconductor band gaps," *Applied Physics Letters*, vol. 58, pp. 2924-2926, 1991.
- [134] D. Babić and R. Tsu, "Excitons in silicon nanocrystallites," *Superlattices and microstructures*, vol. 22, pp. 581-588, 1997.
- [135] M. Baldo, S. Lamansky, P. Burrows, M. Thompson, and S. Forrest, "Very high-efficiency green organic light-emitting devices based on electrophosphorescence," *Applied Physics Letters*, vol. 75, p. 4, 1999.
- [136] C. Adachi, M. A. Baldo, M. E. Thompson, and S. R. Forrest, "Nearly 100% internal phosphorescence efficiency in an organic light-emitting device," *Journal of Applied Physics*, vol. 90, pp. 5048-5051, 2001.
- [137] M. Segal, M. Baldo, R. Holmes, S. Forrest, and Z. Soos, "Excitonic singlet-triplet ratios in molecular and polymeric organic materials," *Physical Review B*, vol. 68, p. 075211, 2003.
- [138] H. Uoyama, K. Goushi, K. Shizu, H. Nomura, and C. Adachi, "Highly efficient organic light-emitting diodes from delayed fluorescence," *Nature*, vol. 492, pp. 234-238, 2012.
- [139] K. Goushi, K. Yoshida, K. Sato, and C. Adachi, "Organic light-emitting diodes employing efficient reverse intersystem crossing for triplet-to-singlet state conversion," *Nature Photonics*, vol. 6, pp. 253-258, 2012.
- [140] M. A. Baldo, C. Adachi, and S. R. Forrest, "Transient analysis of organic electrophosphorescence. II. Transient analysis of triplet-triplet annihilation," *Physical Review B*, vol. 62, p. 10967, 2000.
- [141] J. Wilson, A. Dhoot, A. Seeley, M. Khan, A. Köhler, and R. Friend, "Spin-dependent exciton formation in  $\pi$ -conjugated compounds," *Nature*, vol. 413, pp. 828-831, 2001.
- [142] C. Adachi, M. A. Baldo, S. R. Forrest, and M. E. Thompson, "High-efficiency organic electrophosphorescent devices with tris (2-phenylpyridine) iridium doped into electron-transporting materials," *Applied Physics Letters*, vol. 77, pp. 904-906, 2000.

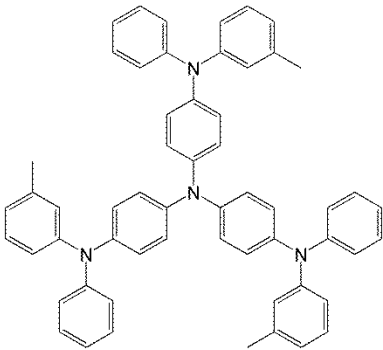
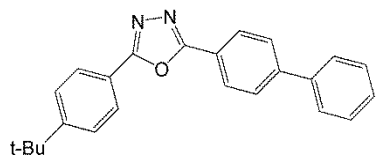
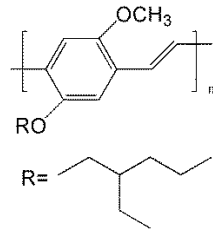
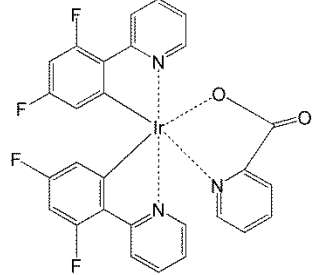
- [143] P. Calcott, K. Nash, L. Canham, M. Kane, and D. Brumhead, "Identification of radiative transitions in highly porous silicon," *Journal of Physics: Condensed Matter*, vol. 5, p. L91, 1993.
- [144] T. Förster, "10th Spiers Memorial Lecture. Transfer mechanisms of electronic excitation," *Discussions of the Faraday Society*, vol. 27, pp. 7-17, 1959.
- [145] D. L. Dexter, "A theory of sensitized luminescence in solids," *The journal of chemical physics*, vol. 21, p. 836, 1953.
- [146] W. A. Luhman and R. J. Holmes, "Investigation of energy transfer in organic photovoltaic cells and impact on exciton diffusion length measurements," *Advanced Functional Materials*, vol. 21, pp. 764-771, 2011.
- [147] S. R. Scully and M. D. McGehee, "Effects of optical interference and energy transfer on exciton diffusion length measurements in organic semiconductors," *Journal of applied physics*, vol. 100, pp. 034907-034907-5, 2006.

## Appendix:

### A.1 Structures of the Chemicals Mentioned in This Thesis

Short name	Full name	Chemical structure
PPV	poly-(para-phenylenevinylene)	
PEDOT:PSS	poly(3,4-ethylenedioxythiophene):poly(styrenesulfonate)	
poly-TPD	poly(4-butylphenyl-diphenyl-amine) (poly-TPD)	
Alq <sub>3</sub>	tris(8-hydroxyquinolato) aluminum	

TCTA	4,4',4''-tris-(N-carbazolyl)-triphenylamine	
CBP	4,4'-Bis( <i>N</i> -carbazolyl)-1,1'-biphenyl	
PVK	Poly(9-vinylcarbazole)	
Ir(ppy) <sub>3</sub>	Tris[2-phenylpyridinato-C <sup>2</sup> ,N]iridium(III)	
4CzIPN	(2,4,5,6-tetrakis(carbazol-9-yl)-1,3-dicyanobenzene)	

m-MTDATA	4,4',4''-Tris(N-3-methylphenyl-N-phenylamino)triphenylamine	
t-Bu-PBD	2-(4'-biphenyl)-5-4''-tert-butylphenyl)-1,3,4-oxadiazole	
MEH-PPV	Poly[2-methoxy-5-(2-ethylhexyloxy)-1,4-phenylenevinylene]	
Flrpic	Bis[2-(4,6-difluorophenyl)pyridinato-C2,N](picolinato)iridium(III)	
UGH2	triphenyl-(4-triphenylsilylphenyl)silane	